1 **Using stable isotopes (δ^{17}O, δ^{18}O and δD) of gypsum hydration**

2 **water to ascertain the role of water condensation in the formation**

3 **of subaerial gypsum speleothems**

4 Fernando Gázquez[1*], José María Calaforra[2], Nicholas P. Evans[1] and David A.

5 Hodell[1]

6 [1]Godwin Laboratory for Palaeoclimate Research, Department of Earth Sciences, University of

7 Cambridge, Downing Street, Cambridge, CB2 3EQ (United Kingdom)

8 [2]Water Resources and Environmental Geology Research Group. University of Almería. Ctra.

9 Sacramento s/n, 04120, Almeria (Spain)

10 *corresponding author

11 **Abstract**

12 We analyzed the stable isotopes (δ^{17}O, δ^{18}O and δD) of gypsum hydration water

13 (GHW) in a variety of speleothems, as well as condensation and infiltration waters in

14 five caves of the semiarid gypsum karst of Sorbas basin (Almeria, SE Spain).

15 Microclimate parameters (air temperature, relative humidity and effective

16 condensation rate) were also monitored over an annual cycle. We found that the

17 mother solution from which the majority of gypsum speleothems grow is composed

18 of a mixture of condensation (~60%) and infiltration water (~40%) that undergoes

19 evaporation. Although evaporation of infiltration water alone was thought to be

20 responsible for secondary gypsum precipitation in vadose caves, our results suggest

21 that condensation can be a major source of water for the formation of gypsum

22 speleothems. The modelled d-excess and Δ^{17}O trajectories of water during the

23 evaporative process confirm that the majority of speleothems precipitate from a

24 mixture of condensation and infiltration water under relative humidity of 75-85%,

similar to that measured in the cave atmosphere during winter. These findings have important implications for future studies of gypsum speleothems as paleoenvironmental archives.

Keywords: gypsum hydration water, stable isotopes, gypsum speleothems, condensation, gypsum caves.

1. Introduction

Most studies that have examined gypsum karst have focused on their geomorphological characteristics and formation mechanisms (Forti and Sauro, 1996; Klimchouk et al., 1996; Calaforra and Pulido-Bosch, 1996, 1997, 1999, 2003; Gutierrez and Cooper, 2013), hydrogeology (e.g. Calaforra and Pulido-Bosch, 1999; Klimchouk and Aksem, 2002; Sanna et al., 2012; Acero et al., 2013) and geological hazards (Benito et al., 1995; Klimchouk and Andrejchuk, 1996; Galve et al., 2008, 2009; Cooper and Gutierrez, 2013, among others). While these aspects of gypsum karst have been thoroughly investigated, less attention has been paid to other aspects, including subterranean microclimate (Fernandez-Cortés et al., 2006; Gázquez et al., 2015a, b) and the genesis of gypsum speleothems (Calaforra, 1998; Forti, 1996; Gázquez and Calaforra, 2014; Gázquez et al., 2015a).

Subaerial gypsum speleothems are known to form in gypsum caves located in arid or semiarid environments, where conditions are generally warm and dry. These include the caves of the gypsum karst of Sicily, Italy (Madonia et al., 2011; Di Maggio et al., 2012), New Mexico, United States (Calaforra and Forti, 1994; Doran and Hill, 1998) and Sorbas basin, SE Spain (Gázquez and Calaforra, 2014). In gypsum karst

48   located in wetter climates (e.g. Emilia Romagna, Northern Italy), gypsum

49   speleothems are rare, especially when compared with the presence of calcite

50   speleothems (Forti, 1996; Calaforra et al., 2008; Columbu et al., 2015).

51   Gypsum speleothem precipitation has traditionally been explained by the dissolution

52   of the gypsum bedrock by infiltration water and subsequent evaporation of calcium-

53   sulfate-rich solution in subaerial conditions (Forti, 1996). However, recent

54   investigations suggest that condensation water may be important for subaerial

55   speleogenesis in gypsum caves of semiarid areas, as well as for the precipitation of

56   secondary gypsum in caves (Gázquez et al., 2015a). Indeed, condensation is known

57   to be an important speleogenetic agent that controls the development and

58   morphologic characteristics of dozens of limestone caves worldwide (Jameson,

59   1991; Tarhule-Lips and Ford, 1998; De Freitas and Schmekal, 2006; Cigna and

60   Forti, 1986; Bakalowicz et al., 1987; Sarbu and Lascu, 1997; Audra et al., 2007;

61   Gázquez et al., 2013; 2015a, among others). For limestone cave, this mechanism is

62   known as "condensation-corrosion", which is especially efficient in causing the

63   dissolution of carbonates when CO_2 diffuses into condensation water (Ford and

64   Williams, 2007).

65   Unlike carbonates, atmospheric CO_2 concentration does not affect the kinetics of

66   gypsum dissolution. Instead, condensation plays an important role because gypsum

67   is about ten times more soluble than calcite (Wigley, 1973). Because carbonic acid is

68   not involved in gypsum dissolution, the term "condensation-corrosion" is not

69   appropriate for gypsum caves; instead, we refer to the process as "condensation-

70   solution".

Gypsum speleothems are potential paleoenvironmental archives due to the particular conditions under which they form (Calaforra et al., 2008; Gázquez et al., 2011). However, a lack of understanding regarding their genesis has limited their use as a paleoclimate proxy to date. Stable isotopes in gypsum hydration water (GHW) of speleothems are useful for understanding how they form and reconstructing past changes in the isotopic composition of waters in hydrothermal caves (Gázquez et al., 2013). Provided that GHW has not undergone post-depositional isotopic exchange or re-precipitation, the isotopic composition of the original mother water can be determined by applying known fractionation factors (Gonfiantini and Fontes, 1963; Fontes and Gonfiantini, 1967; Sofer, 1978; Hodell et al., 2012; Gázquez et al., 2017). To interpret the isotopic signatures of GHW from gypsum speleothems, a precise understanding of the origin of the mother water (i.e. condensation vs. infiltration water) is necessary.

Here, we evaluate the importance of condensation water in the formation of gypsum speleothems in gypsum caves of semi-arid regions by measuring stable isotopes ($\delta^{17}O$, $\delta^{18}O$ and δD) of GHW in a selection of gypsum speleothems (gypsum coralloid, frostwork, stalactites, crystals formed in the sediment, etc.) from five shallow caves/passages in the gypsum karst of Sorbas (SE Spain). These results have been compared with those of condensation and infiltration waters in the caves, and rain and spring waters in the karst of Sorbas basin. Furthermore, microclimate parameters (air temperature, relative humidity and effective condensation rate) were monitored over an annual cycle to determine the conditions under which secondary gypsum forms. We discuss how variations in microclimate lead to the genesis of gypsum speleothems within the cave system, and propose a mechanism to explain the geochemical results observed in dripwater and gypsum hydration water.

96

2. Geological and climatic setting

The gypsum karst of Sorbas is located in the Tabernas-Sorbas basin, SE Spain. It lies within a topographic depression bounded to the north by the Filabres range and to the south by the Alhamilla and Cabrera ranges (Fig. 1). The sedimentary infill of this intramontane Neogene basin contains significant Messinian gypsum deposits (Dronkert, 1977; Krijgsman et al., 2001; Evans et al., 2015, among others). The karstified Messinian gypsum (Yesares Member) occurs within a 120-m thick cyclic sequence consisting of alternating gypsum and carbonate marl (Dronkert, 1977). The selenitic gypsum units are up to 30 m thick.

Over one thousand cave entrances have been recognized in only 12 km^2 in the gypsum karst of Sorbas. The length of its surveyed underground network is over 100 km. We focus our investigation on speleothems from the upper passages of Covadura Cave (Upper and Lower Bosque Galleries and Nieves Gallery); the C3 Cave; the Sima Fé Cave (all three of which are located in the northern sector of the of Sorbas basin); and a cave near the El Peral-Majadas Viejas quarry (located in the southern sector of the Sorbas basin) (Fig. 1a). These cavities contain outstanding examples of gypsum speleothem formation (Gázquez and Calaforra, 2014; see the supplementary material for additional geomorphological details of these caves). Relatively intense airflow within the galleries promotes evaporation; this produces subaerial gypsum precipitation in the form of speleothems (Calaforra et al., 2008; Gázquez and Calaforra, 2014; Gázquez et al., 2015).

Sorbas is a semi-arid zone, with an average annual temperature of 19ºC (with a January minimum average of 11ºC and a July maximum of 30ºC) and a mean annual

120   rainfall of 210 mm (minimum monthly mean in July and maximum in November). The

121   estimated annual potential evapotranspiration for Sorbas is 1190 mm yr^{-1} (John and

122   Harris, 2011), nearly five times the mean annual precipitation. Some 80% of the

123   annual rainfall occurs during infrequent storm events, usually in the autumn

124   (Esteban-Parra et al., 1998; Gázquez et al., 2015b). The gypsum karst is drained by

125   six springs, namely El Peral, Molinos, Viñicas-Cueva del Agua, Fortuna-Cueva del

126   Yeso, APAS Cave and El Tesoro Cave (Fig. 1a; Sanna et al., 2012), most of which

127   remain active throughout the year.

128

129   **3. Materials and Methods**

130   **3.1. Speleothems and water sampling**

131   Gypsum speleothems samples were collected during several surveys between 2012

132   and 2015. Twenty-five samples were selected on the basis of their morphologies and

133   expected formation mechanisms (Gázquez and Calaforra, 2014). This includes

134   popcorn-type speleothems (globular concretions made of microcrystalline gypsum),

135   gypsum crusts (planar coatings made of microcrystalline gypsum), hollow

136   stalagmites (Calaforra and Forti, 1990), gypsum frostwork, stalactites, coralloids

137   (aggregates of fibrous gypsum crystals resembling a coral), gypsum needles grown

138   in fluviokarstic detrital sediments deposited on the cave walls, gypsum trays

139   suspended from the cave ceiling, cone-shaped aggregated of gypsum crystals

140   known as "Christmas trees", and finally a gypsum flowstones from a cave intercepted

141   by the mining activities in the El Peral-Majadas Viejas quarry (see supplementary

142   information for detailed descriptions of the samples and locations).

143   Rainwater samples (n=24), spring waters (n=15), condensation water in caves

144   (n=11), dripwater from points with constant slow dripping (called dripwater hereafter;

145   n=35) and from fast discharge points (called infiltration-discharge hereafter; n=2)

146   were collected between September 2009 and June 2013 (see supplementary

147   information for addition details about the sampling method and locations).

148

149   **3.2. Isotopic analysis of gypsum hydration water and waters**

150   GHW from speleothems samples was extracted by slowly heating each sample

151   (~200 mg) to 400°C, *in vacuo,* using a bespoke offline extraction system consisting

152   of six vacuum lines contained within a modified gas chromatography (GC) oven,

153   following the methods of Gázquez et al. (2015c). Prior to the extraction, powdered

154   gypsum samples were dried in an oven overnight at 45°C.

155   Oxygen ($\delta^{18}O$) and hydrogen (δD) isotopes and hydration water of 8 speleothems

156   samples were measured simultaneously by cavity ring down spectroscopy (CRDS) in

157   the Godwin Laboratory at the University of Cambridge (United Kingdom) using a

158   L1102-i Picarro water isotope analyzer (Hodell et al., 2012). In addition, the GHW of

159   17 samples was measured using a L2140-i Picarro CRDS analyzer, which is capable

160   for the analysis of triple oxygen (^{16}O, ^{17}O, ^{18}O) and hydrogen (H, D) isotopes (Steig

161   et al., 2014). All results are reported in parts per thousand (‰) relative to V-SMOW.

162   External error (1SD) of the method was ±0.05‰ for $\delta^{17}O$, ±0.1‰ for $\delta^{18}O$, ±0.7‰ for

163   δD, ±0.8‰ for d-excess and ±11 per meg (±0.011‰) for $\Delta^{17}O$, as estimated by

164   repeated analysis (n=5) of an analytical grade standard, extracted together with five

165   samples in each run (Gázquez et al., 2015c) (see supplementary material for

166   additional details).

167   Eighteen rainwater samples, 35 dripwater/discharge samples and 3 condensation

168   samples collected from February 2010 to June 2012 were analyzed for $\delta^{18}O$ and δD

169   using a Laser Water Isotope Analyzer V2 (Los Gatos Research, Inc., Mountain View,

170   CA, USA) at the Stable Isotope Facility of University of California (Davis, CA, USA).

171   Internal standards were calibrated against V-SMOW, GISP, and SLAP and typical

172   internal precision (1SD) was better than ±0.3 for $\delta^{18}O$ and ±2 per mil for δD. The rest

173   of the samples (6 rainwater, 9 dripwater, 8 condensation water and 15 spring water

174   samples) were analyzed using the same L2140-i Picarro CRDS analyzer described

175   for the analysis of GHW in the Godwin Laboratory, University of Cambridge.

176

177   **3.3. Microclimate monitoring**

178   Microclimate parameters (air temperature and humidity) in the Upper Bosque (S1),

179   Lower Bosque (S2) and Nieves Gallery (S3) of Covadura Cave were monitored by

180   using dataloggers manufactured by iButton® of Maxim-ic (model DS1923-F5) at the

181   locations indicated in Fig. 2 (see supplementary material for additional details of

182   microclimate monitoring). Climatic parameters outside the cave were also measured

183   using the same device for the period September 2012 to November 2013.

184

185   **4. Results**

186   **4.1. Stable isotopes in gypsum hydration water**

187   Twenty-five samples representing different types of gypsum speleothems were

188   analysed for stable isotopes of GHW (Table 1). The measured $\delta^{17}O$ values of GHW

189   range from -1.0‰ to 3.1‰, $\delta^{18}O$ from -2.3‰ to 5.9‰ and δD from -59.7‰ to -

190   16.9‰. The d-excess values of the mother water range from -15.5‰ to 8.5‰,

191   whereas the $\Delta^{17}O$ ranges from -53 per meg to 30 per meg, and their values are

192   negatively correlated with those of the $\delta^{18}O$ across the dataset.

193

194   **4.2. Stable isotopes in rain and caves waters**

195   The local meteoric water line (LMWL) in the Sorbas area was calculated to be δD =

196   7.2 $\delta^{18}O$ + 7.2 using the values of the rain and spring waters (Table 2). When plotting

197   $\delta^{18}O$ vs δD of the condensation water in Covadura Cave (Table 3), the values fall on

198   the upper part of the LMWL (Fig. 3). During the time of this study, effective

199   condensation (i.e. condensation minus possible evaporation of the condensed water)

200   occurred between December and June (up to 15 $cm^3m^{-2}day^{-1}$), whereas no

201   condensation water was recovered between January and May (Fig. 4 and Table 2).

202   When plotting $\delta^{18}O$ vs δD, the dripwater (slow discharge) values fall on the upper

203   part of the LMWL, along a line with the expression: δD= 7.6 $\delta^{18}O$ + 11.6. The amount

204   of water collected and the water conductivity of the water recovered during each

205   sampling period show a weak positive correlation (R^2=0.42). The water collected

206   from the ephemeral, fast, infiltration-discharge points show $\delta^{18}O$ and δD values

207   similar to the mean of the rain and the springs (Table 3).

208

209   **4.3. Microclimate monitoring**

210   The highest daily mean temperatures in the subterranean atmosphere occurred in

211   September in the Nieves and Upper Bosque Galleries, with values of up to 22.5 °C in

212 the Upper Bosque Gallery (Table 4). We observed that from November to April, the

213 external daily mean air temperature outside approaches that of the cave

214 atmosphere. On occasion, the external temperature fell below that of the internal

215 cave atmosphere (Fig. 5 and Table 4).

216 The relative humidity in the Lower Bosque Gallery shows a seasonal pattern with

217 relatively constant values close to 100% between May and December, and lower

218 and more variable values between January and April (91±5%). The measured values

219 were as low as ~70% and maintained almost constant levels during several days in

220 February. This pattern has also been observed in the Upper Bosque Gallery, with

221 relative humidity of ~100% in July and August, and periods of almost constantly low

222 relative humidity of ~65% in January and February (Fig. 5).

223

224 **5. Discussion**

225 **5.1. Seasonal patterns of water condensation driven by cave microclimate**

226 There are a number of dissolution morphologies in the caves of the gypsum karst of

227 Sorbas that suggest the presence of active condensation and dissolution

228 mechanisms. These include rounded and smoothed surfaces, bell-shape

229 condensation cupolas and pendant-like features. These forms appear on the ceiling

230 of the shallower passages of Covadura Cave, Cueva del Agua Cave and C3 Cave

231 (Gázquez et al., 2015a). Indeed, condensation-solution has been found to be an

232 important process involved in the subaerial speleogenesis in these caves, producing

233 erosion rates of the cave surfaces of up to 0.033 mm/yr (Gázquez et al., 2015a).

234   As shown in Figures 4 and 5, active condensation in Covadura Cave takes place

235   between June and December (up to 15 $cm^3m^{-2}day^{-1}$, after considering the

236   dimensions of the collector), whereas no condensation water was recovered

237   between January and May. This seasonal pattern is intrinsically linked to the

238   temperature disequilibria between the external and internal cave atmosphere. The

239   cave air temperature remains relatively constant throughout the year (e.g.

240   13.9±1.9^{o}C in the Lower Bosque Gallery); however, the daily external air

241   temperature is considerably higher in summer (i.e. up to 29°C), but sporadically

242   lower than the cave atmosphere in winter (i.e. occasional daily means of 5°C) (Fig. 6,

243   Table 4).

244   During the warmer period (from March to November), the karstic system acts as a

245   cold air trap and there is little exchange of cave air with the external atmosphere.

246   This partial isolation is driven by the density contrast between the warmer external

247   air and the colder cave atmosphere (Fig. 6a). On occasion, "heat waves" during

248   summer can be transmitted to the cave atmosphere. This has been observed in the

249   Upper Bosque Gallery, likely due to external wind and atmospheric pressure

250   changes that force changes in cave air circulation and/or atmospheric pressure

251   (Fernández-Cortés et al., 2008). The partial isolation of the cave from the external

252   atmosphere from March to November causes the cave atmosphere to reach its

253   highest annual relative humidity of up to 100%. These high relative humidity

254   conditions favour water condensation on cave surfaces, as observed in the Upper

255   and the Lower Bosque galleries. The opposite climatic conditions prevail between

256   January and May when colder (12.4±4.3^{o}C) and relatively dry (68±16%) air masses

257   flow into the cave, leading to drier conditions in the subterranean atmosphere (75-

258   85%) (Fig. 6b). This scenario favors evaporation over condensation.

259 The efficiency of the dissolution-precipitation processes in different parts of the cave

260 is likely controlled by the degree of thermal disequilibrium between the external air

261 and the colder cave surfaces. At equal depth below the surface, for example, the

262 temperature of the inner part of the Nieves Gallery is ~4°C lower than in the Upper

263 Bosque Gallery (Table 4). The colder temperature in the inner part of the Nieves

264 Gallery could favor a greater condensation rate than in the outermost part of this

265 passage. These temperature differences could dictate the relative contributions of

266 condensation and infiltration water that form speleothems in different parts of the

267 cave.

268 Condensation water has relatively low ionic content, as deduced from its low

269 electrical conductivity (283±135 μS), and so has the ability to dissolve gypsum (up to

270 2.4 g/l at 15°C; Blount and Dickson, 1973). Under the relatively dry atmospheric

271 conditions observed during the colder months, water (either condensed or infiltrated

272 water) can evaporate and lead to formation of gypsum speleothems.

273

274 **5.2. Sources of water to drip points within the cave system**

275 The δ^{18}O and the δD values of condensation waters from the caves of the gypsum

276 karst of Sorbas (Fig. 3) plot at the upper extreme and slightly above the LMWL (Fig.

277 3). The offset above the LMWL can by explained by the presence of "occult rain"

278 within the cave system. "Occult rain", an important mechanism of water recharge in

279 low-humidity regions, occurs due to the re-evaporation of local water and

280 subsequent condensation of vapor on vegetation and soils (e.g. Aravena et al.,

281 1989). If such vapor is re-condensed in any significant quantity before mixing with

282 the larger tropospheric reservoir, the isotopic composition of the resulting

283   condensation water will fall slightly above the LMWL, along a condensation line with

284   a slope similar to the LMWL (Ingraham and Matthews, 1988, 1990; Clark and Fritz,

285   1997). This is observed in the measured condensation water ^{18}O and the δD. The

286   measured condensation water line is defined by the equation $\delta D= 6.1 \, \delta^{18}O + 5.2$, the

287   gradient of which is less than that of the LMWL ($\delta D= 7.2 \, \delta^{18}O + 7.2$). This shallower

288   slope suggests that small amounts of evaporation occurred from the condensing

289   water droplets on the metal plate or in the water collector before sampling, a process

290   that is likely to occur at the beginning and end of the periods over which

291   condensation is present (i.e. April and January, respectively).

292   The $\delta^{18}O$ and δD of the dripwater plots between values of condensation water and

293   those of the infiltration water (springs) in the Sorbas aquifer. The dripwater lies on a

294   line ($\delta D= 7.6 \, \delta^{18}O + 11.6$) above the LMWL ($\delta D= 7.2 \, \delta^{18}O + 7.2$), and the d-excess

295   of the dripwater (13.4±2.3‰) is higher than that of the infiltration waters in the

296   Sorbas aquifer (9.9±2‰). This suggests re-evaporation of water and condensation

297   inside the cave partially controls the isotopic composition of dripwater in the Sorbas

298   caves. In this case, the source of water vapour is wet air from deepest part of the

299   cave, or moisture transported by the limited air masses entering the cave during the

300   warmer period.

301   The relative contribution of each water source (infiltration vs condensation) to the

302   dripwater can be calculated assuming a two-endmember mixing line between the

303   condensation water (endmember values of -2.7±0.6‰ and -11.4±4.0‰ for $\delta^{18}O$ and

304   δD, respectively) and the infiltration water (endmember values of -5.2±0.4‰ and -

305   31.9±2.9‰ for $\delta^{18}O$ and δD, respectively). Calculations indicate the contribution of

306 the condensation source to the dripwater is ~63%, whereas infiltration water

307 represents ~37%.

308 The electrical conductivity of dripwater is considerably lower than that of waters

309 measured in the springs and the infiltration-discharge points in the cave. Considering

310 the waters from the both the karstic outlets and the fast, ephemeral discharges have

311 circulated through the epikarst, the relatively low conductivity of the dripwater clearly

312 indicates mixing of infiltration water (>2.3 mS cm) and condensation water (<0.5 mS

313 cm) (Fig. 7). This result corroborates the interpretation inferred from the $\delta^{18}O$ and δD

314 values. The $\delta^{18}O$ also shows a negative correlation with the conductivity of dripwater,

315 suggesting that the relative contributions of condensation and infiltration water to the

316 dripwater could have varied over the time of this study. This is also shown by the

317 lower values of conductivity in dripwater measured during May to November 2011

318 (1.82±0.09 mS cm), compared with those measured during the same period in 2012

319 (2.21±0.12 mS cm) (Table 3). Equally, there was less rainfall during May to

320 November 2011 (123 mm) than during the same period in 2012 (183 mm).

321 Therefore, the infiltration in 2012 would likely have been lower than in 2011, thus the

322 contribution of infiltration water may have been less significant compared to that of

323 condensation water. This also corroborates the higher values of $\delta^{18}O$ and δD

324 observed in dripwater during 2011, compared to 2012.

325

326 **5.3. Isotopic composition of water forming speleothems and implications for**

327 **paleoclimatic studies**

328   The oxygen and hydrogen isotope composition of the parent water from which the

329   gypsum formed is calculated by using the values of GHW and known fractionation

330   factors (α):

$$\alpha_{gypsum-water} = \frac{\delta_{gypsum} + 1000}{\delta_{water} + 1000}$$

331   Equation 1,

332   where δ_{gypsum} and δ_{water} denote the isotopic deviation (i.e. $\delta^{17}O$, $\delta^{18}O$ and δD) of the

333   hydration water and mother water with respect to V-SMOW. These fractionation

334   factors have been recently revised by Gázquez et al. (2017) who obtained more

335   precise and accurate values than previous studies (Gonfiantini and Fontes, 1963;

336   Fontes and Gonfiantini, 1967; Sofer, 1978; Hodell et al., 2012). The fractionation

337   factors for oxygen isotopes ($\alpha^{17}O_{gypsum-water}$ and $\alpha^{18}O_{gypsum-water}$) are largely unaffected

338   by different temperatures between 5 and 30°C (Gázquez et al., 2017). The

339   fractionation factor for hydrogen ($\alpha D_{gypsum-water}$) increases slightly (from 0.9787 to

340   0.9813) in the same temperature range. We use $\alpha^{18}O_{gypsum-water}$ and $\alpha D_{gypsum-water}$ at a

341   temperature of 15°C (Gázquez et al., 2017), representing the mean temperature in

342   the upper galleries of Covadura Cave (Table 4). Thus, $\alpha^{18}O_{gypsum-water}$ of 1.00355 and

343    $\alpha D_{gypsum-water}$ of 0.979 are used. Changes in temperature of ±5°C, similar to the range

344   observed in the investigated caves, result in uncertainty of ±0.5‰ in the calculated

345   values of δD of the mother water, which is insignificant given the analytical precision

346   of the measurements (±0.7‰).

347   The relation between $\alpha^{17}O_{gypsum-water}$ and $\alpha^{18}O_{gypsum-water}$ is given by the parameter θ

348   (Mook, 2000):

349 $$\alpha^{17}O_{gypsum\text{-}water} = \alpha^{18}O_{gypsum\text{-}water}^{\theta} \quad \text{(Equation 2)}$$

350 This parameter has been found to be 0.5297±0.0012 and is insensitive to

351 temperature between 3 and 55°C (Gázquez et al., 2017). Therefore, we use

352 $\alpha^{17}O_{gypsum\text{-}water}$ of 1.00188.

353 According to their isotopic compositions, the samples can be divided into two distinct

354 groups on the basis of their $\delta^{18}O$ and δD values (Fig. 3): the first group comprises

355 samples with relatively depleted values that lie on the local meteoric water line

356 (LMWL). This includes the gypsum needles grown in clayey sediments in C3 Cave

357 and the gypsum flowstone collected in the vicinity of the El Peral-Majadas Viejas

358 quarry. The second group contains samples of gypsum coralloids, crusts, "Christmas

359 trees", frostwork, popcorn, stalactites and hollow stalagmites. This second group

360 plots on an evaporation line with slope of 3.2 (Fig. 3).

361 The deviation of the formation waters with respect to the global meteoric water line

362 (GMWL) can be expressed by the parameters d-excess and $\Delta^{17}O$. The d-excess is

363 defined as:

364 $$d\text{-excess} = \delta D - 8\,\delta^{18}O \quad \text{(Equation 3)}$$

365 Where $\delta^{18}O$ and δD represent the isotopic composition of water and 8 is the slope of

366 the GMWL (Dansgaard, 1964). In our study, we define $\Delta^{17}O$ as:

367 $$\Delta^{17}O = \ln(\delta^{17}O + 1) - 0.528\ln(\delta^{18}O + 1) \quad \text{(Equation 4)}$$

368 Where $\delta^{17}O$ and $\delta^{18}O$ denote the isotopic composition of water and 0.528 is used as

369 the reference *C* value, as also utilized in previous studies on triple oxygen isotopes

370 in the hydrologic cycle (Barkan and Luz, 2007; Luz and Barkan, 2010; Schoenemann

371 et al., 2013; Steig et al., 2014; Surma et al., 2015; among others). The parameter

372 $\Delta^{17}O$ is equivalent to the term $^{17}O_{excess}$ coined by Barkan and Luz (2007). The $\Delta^{17}O$

373 of waters decreases with the degree of evaporation of water (i.e., a decrease in ^{17}O

374 with respect to the trajectory defined by meteoric waters) (Luz and Barkan, 2010;

375 Steig et al., 2014; Surma et al., 2015).

376 The $\delta^{18}O$ and δD of the solutions that formed most of the speleothems in the present

377 study plot on an evaporation line ($\delta D = 3.2 \, \delta^{18}O -5.7$) that intercepts the LMWL at

378 $\delta^{18}O$ of -3.9‰ and δD of -18.1‰. These values match those of dripwater

379 (condensation + infiltration) measured in the cave ($\delta^{18}O$ of -3.8±0.7‰ and δD of -

380 17.0±6.4‰). This strongly suggests that these speleothems form from evaporated

381 water that is a mixture of condensation (~60%) and infiltration (~40%) water. This is

382 also shown by plotting $\delta^{18}O$ versus d-excess and $\Delta^{17}O$ (Fig. 8). $\delta^{18}O$ is negatively

383 correlated with both parameters, as expected for evaporation (Gat, 1996; Luz and

384 Barkan, 2010). However, the starting point of the evaporation process is not the

385 mean value of rainwater or the infiltration water (springs), but the mean value of the

386 slow dripwater (infiltration/condensation) in the cave.

387 We model the evaporation trajectories of different types of water in the karst

388 (condensation, fast infiltration and dripwater) using an isotopic mass balance

389 equation (Criss, 1999; Surma et al., 2015). We consider the liquid water in contact

390 with the speleothems (water films, drops or water in interstitial spaces between

391 crystals) as a finite water pool with inflow (condensation and/or infiltration), outflow

392 (water migration by capillarity or gravity, etc.) and water loss by evaporation.

393 The isotopic evolution of water during evaporation (e.g. $\delta^{18}O$ vs $\Delta^{17}O$ and $\delta^{18}O$ vs d-

394 excess) depends on the isotopic composition of the initial water (inflow) and the

395   outflow (if any), the temperature, the relative humidity, the isotopic composition of the

396   water vapour in equilibrium with the liquid water and the ratio of water loss by

397   evaporation with respect to outflow. This process can be described by the

398   expression (Criss, 1999):

$$^{*}R_{WS} = \frac{^{*}\alpha_{evap}^{0} \cdot (1-h) \cdot {}^{*}R_{WI} + {}^{*}\alpha_{eq}^{0} \cdot h \cdot X_E \cdot R_V}{X_E + {}^{*}\alpha_{evap}^{0} \cdot (1-h) \cdot (1-X_E)}$$

399   (Equation 5)

400   Where $^{*}R_{WS}$ is the isotopic ratio (e.g. $\delta^{18}O+1000$) of the evaporated water. $^{*}\alpha^{0}_{evap}$ is

401   the effective fractionation factor, calculated as a product of the equilibrium

402   fractionation factor ($^{*}\alpha^{0}_{eq}$) and the diffusive fractionation factor ($^{*}\alpha^{0}_{diff}$) between the

403   water and the vapour. The parameter h is the relative humidity of air (0 to 1). R_{WI} is

404   the isotopic ratio of the initial solution, R_v is the isotopic ratio of the vapour and X_E

405   represents the fraction of water loss by evaporation with respect to the outflow from

406   the system (e.g. X_E=0 meaning no evaporation and X_E=1 all water loss by

407   evaporation). This model assumes isotopic equilibrium between the liquid water and

408   the vapour phase and homogeneous isotopic composition of both reservoirs. Also,

409   pure diffusion is assumed because laminar flow is expected to prevail over turbulent

410   flow in the cave atmosphere.

411   We calculate $^{*}\alpha^{0}_{eq}$ as a function of temperature using the equations of Horita and

412   Wesolowski (1994), for temperature of 15°C (mean cave temperature). Then, we use

413   $\alpha^{18}O^{0}_{eq}$ of 1.00794, αD^{0}_{eq} of 1.09059. $\alpha^{17}O^{0}_{eq}$ is calculated as $\alpha^{17}O^{0}_{eq} = \alpha^{18}O^{0}_{eq}{}^{\theta}$,

414   where θ is 0.529 (Barkan and Luz, 2005). $^{*}\alpha^{0}_{evap}$ is obtained as the product of $^{*}\alpha^{0}_{eq}$

415   and $^{*}\alpha^{0}_{diff}$, where $\alpha^{18}O^{0}_{diff}$ is 1.0283, αD^{0}_{diff} is 1.0269 (at 15°C; Luz et al., 2009) and

416    $\alpha^{17}O^0_{diff}$ is calculated as $\alpha^{17}O^0_{diff} = \alpha^{18}O^0_{diff}{}^{\theta}$, where θ is 0.5185 (Landais et al., 2006;

417   Barkan and Luz, 2007).

418   The modelled evaporation trajectories for $\delta^{18}O$ vs d-excess and $\delta^{18}O$ vs $\Delta^{17}O$ match

419   the values of the waters that formed most speleothems in the caves of Sorbas, when

420   R_{WI} is set as the isotopic composition of the slow dripwater (condensation +

421   infiltration) in the cave and relative humidity of 75%-85%, as measured in the

422   subterranean atmosphere. We found that changes in temperature (e.g. ±5°C) do not

423   significantly affect the evaporation trajectories, especially in the case $\delta^{18}O$ vs $\Delta^{17}O$.

424   The values of some samples (i.e. coralloids, frostwork and gypsum crusts) have a

425   better fit to the evaporation trajectory of condensation water than that of dripwater,

426   suggesting a greater proportion of condensation water in the formation of these

427   speleothems. However, only a few samples (stalactites and hollow stalagmites) fit

428   the trajectories for the evaporation of infiltration water modelled for relative humidity

429   of 85% (Fig. 9). Again, this suggests that evaporation of solutions with different

430   proportions of condensation and infiltration water is the main mechanism responsible

431   for the precipitation of most gypsum speleothems in the caves studied.

432   There is a small cluster of gypsum speleothems, including gypsum needles grown in

433   detrital sediments in C3 cave and a gypsum flowstone from the El Peral-Majadas

434   Viejas Cave, that do not match the evaporation trajectory observed for the rest of

435   samples. The waters that formed these speleothems plot on the values of infiltration

436   waters (i.e. spring waters and the mean of the rainwater), suggesting that they

437   formed under conditions of high relative humidity (~100%) with practically no

438   evaporation. The same observation can be made when plotting $\delta^{18}O$ vs d-excess

439   and $\Delta^{17}O$ (Fig. 8).

440 In the case of the formation of gypsum needles, infiltration water diffused through the

441 detrital sediment and resulted in the crystallization of gypsum in the clayey matrix.

442 The solution was enriched in calcium sulphate in the epikarst and flowed through the

443 fluviokarstic deposits in the cave, dissolving detrital particles of calcium carbonate.

444 The dissolution of calcite (or aragonite) supplied Ca^{2+} to the solution, leading to the

445 supersaturation of gypsum and precipitation of crystals in the sediments.

446 The gypsum flowstone in the El Peral-Majadas Viejas Cave formed from infiltration

447 water that was close to saturation with respect to gypsum. This water slowly flowed

448 onto a previously deposited carbonate flowstone under atmospheric conditions in the

449 cave also close to the water vapour saturation. In this case, dissolution of the calcite

450 flowstone provided an additional source of Ca^{2+} to the solution, resulting in gypsum

451 supersaturation without loss of water by evaporation, as indicated by our

452 measurement of GHW.

453 We suggest that the stable isotopes in GHW in speleothems may serve as a proxy to

454 reconstruct changes in the isotopic composition of the mother solution from which

455 gypsum speleothems formed and how this varied with time. This could be achieved

456 by analysing layered gypsum speleothems (i.e. stalagmites, stalactites, flowstones,

457 etc.) with the chronology obtained by uranium-thorium dating (Sanna et al., 2010).

458 The parameters involved in the isotopic mass balance model suggest that there are

459 several factors that influence $\delta^{17}O$, $\delta^{18}O$ and δD and the resultant d-excess and $\Delta^{17}O$

460 in gypsum speleothems. These include the relative contributions of condensation

461 and infiltration water to the dripwater, and more significantly, the relative humidity in

462 the cave. Changes in other parameters (i.e. temperature) have little effect on the

463 isotopic fractionation factors between GHW and the mother solution. Temperature

464 also has little effect on the trajectory of water $\delta^{18}O$- $\Delta^{17}O$ during evaporation, but is

465 instead strongly dependent on the relative humidity (Surma et al., 2015). Therefore,

466 the coupled measurement of $\delta^{18}O$, $\Delta^{17}O$ and d-excess in gypsum hydration water of

467 speleothems could be used to reconstruct changes in the cave relative humidity in

468 the past.

469

470 **6. Conclusions**

471 The stable isotopes of gypsum hydration water can be used to reconstruct the

472 isotopic composition of the mother solution from which gypsum speleothems

473 (stalagmites, stalactites, flowstones, etc.) formed. We found that gypsum

474 speleothems in semi-arid caves form from the evaporation of solutions composed of

475 a mixture of condensation and infiltration water. This contrasts with the prevailing

476 concept that evaporation of infiltration water alone is responsible for secondary

477 gypsum precipitation in vadose caves.

478 The modelled $\delta^{17}O$, $\delta^{18}O$ and δD trajectories of water during the evaporative process

479 and the derived parameters of d-excess and $\Delta^{17}O$ indicate that the majority of

480 speleothems in the investigated caves precipitate under a relative humidity of 75-

481 85%, similar to that measured in the cave during winter. Importantly, we found that

482 changes in other parameters (i.e. temperature) have little effect on the modelled

483 results, especially on the $\delta^{18}O$- $\Delta^{17}O$ relationship. We suggest the coupled

484 measurement of triple oxygen and hydrogen isotopes in gypsum hydration water of

485 speleothems may be used to study past changes in relative humidity in caves. Stable

486 isotopes in hydration water of subaerial gypsum speleothems is a promising tool for

487 paleo-humidity and paleo-hydrological reconstructions.

488

Acknowledgments

497

7. References

Acero, P., Salazar, F. Gutiérrez, J.P. Galve, L.F. Auqué, D. Carbonel, M.J. Gimeno, J.B. Gómez, M.P., Asta A., Yechieli, Y., 2013. Hydrogeochemical characterization of an evaporite karst area affected by sinkholes (Ebro Valley, NE Spain). Geol. Acta 11(4), 389-407.

Aravena, R., Suzuki, O., Polastri. A., 1989. Coastal fogs and their relation to groundwater. Chem. Geol. 79, 83-91.

Audra, Ph., Hoblea, F., Bigot, J.Y., Nobécourt, J.C., 2007. The role of condensation in thermal speleogenesis: study of a hypogenic sulfidic cave in Aix-les-Bains, France. Acta Carsol. 36, 185–194.

Ayuso, I., Calaforra, J.M., Gutiérrez-Labouret, M., Torres, A., 2014. Cuevas y Simas del Karst en yeso de Sorbas. Ed: Espeleo-Club Almería, ISBN: 978-84941725-1-9, 168 pp.

511 Bakalowicz, W.J., Ford, D.C., Miller, T.E., Palmer, A.N., Palmer, M.V., 1987.

512   Thermal genesis of dissolution caves in the Black Hills, South Dakota. Geol. Soc.

513   Am. Bull. 99, 729–738.

514 Barkan, E., Luz, B., 2005. High precision measurements of $^{17}O/^{16}O$ and $^{18}O/^{16}O$

515   ratios in H_2O, Rapid Commun. Mass Spectrom. 19, 3737–3742.

516 Barkan, E., Luz B., 2007. Diffusivity fractionations of $H_2^{16}O/H_2^{17}O$ and $H_2^{16}O/H_2^{18}O$ in

517   air and their implications for isotope hydrology. Rapid Commun. Mass Spectrom.

518   21, 2999-3005.

519 Bao, H., Cao, X., Hayles, J.A., 2016. Triple Oxygen Isotopes: Fundamental

520   Relationships and Applications, Annu. Rev. Earth Planet. Sci. 44, 463-492.

521 Benito, G., Pérez del Campo, P., Gutiérrez-Elorza, M., Sancho, C., 1995. Natural

522   and human-induced sinkholes in gypsum terrain and associated environmental

523   problems in NE Spain. Environ.Geol. 25, 156-164.

524 Blount, C.W., Dickson, F.W., 1973. Gypsum–anhydrite equilibria in systems $CaSO_4$–

525   H_2O and $CaSO_4$–NaCl–H_2O. Am. Mineral. 58, 323–331.

526 Calaforra, J.M., 1998. Karstología de yesos. PhD thesis, University of Granada

527   (Spain), p 388,

528 Calaforra, J.M., Forti, P., 1990. Le palle di gesso e le Stalagmiti cave: due nuove

529   forme di concrezionamento scoperte nelle grotte di Sorbas (Andalusia, Spagna).

530   Le Grotte d'Italia 15, 73-88.

531 Calaforra, J.M., Forti, P., 1994. Two new types of gypsum speleothems from New

532   México: gypsum trays and gypsum dust. Natl. Speleol. Soc. Bull. 56, 32–37.

533 Calaforra, J.M., Pulido-Bosch, A., 1996. Some examples of gypsum karst and the

534   most important gypsum caves in Spain. Int J Speleol. 25, 225–237.

535 Calaforra, J.M., Pulido-Bosch, A. 1997. Peculiar landforms in the gypsum karst of

536 Sorbas (Southeastern Spain). Carbonates Evaporites 12, 110–116.

537 Calaforra, JM, Pulido-Bosch, A., 1999. Genesis and evolution of gypsum tumuli.

538 Earth Surf. Proc. Land. 24, 919–930.

539 Calaforra JM, Pulido-Bosch A, 2003. Evolution of the gypsum karst of Sorbas (SE

540 Spain). Geomorphology 50, 173-180.

541 Calaforra J.M., Forti P., Fernández-Cortés, A. 2008. Speleothems in gypsum caves

542 and their palaeoclimatological significance. Environ. Geol. 53, 1099–1105.

543 Cigna, A., Forti, P., 1986. The speleogenetic role of airflow caused by convection. 1st

544 contribution. Int. J. Speleol. 15, 41–52.

545 Clark, I.D, Fritz, P., 1997. Environmental Isotopes in Hydrogeology. Lewis

546 Publishers. USA.

547 Columbu, A., De Waele, J., Forti, P., Montagna, P., Picotti, V., Pons-Branchu E.,

548 Hellstrom, J., Bajo, P., Drysdale R., 2015. Gypsum caves as indicators of climate-

549 driven river incision and aggradation in a rapidly uplifting region. Geology 43 (6)

550 539-542.

551 Cooper, A.H., Gutiérrez, F., 2013. Dealing with gypsum karst problems: hazards,

552 environmental issues and planning. In: Frumkin A (ed) Treatise on

553 geomorphology. Karst geomorphology, vol 6. Elsevier, San Diego, pp 451–461.

554 Criss, R.E., 1999. Principles of Stable Isotope Distribution, Oxford Univ. Press,

555 Oxford, U. K.

556 Dansgaard, W., 1964. Stable isotopes in precipitation. Tellus, 16(4), 436–468.

557 De Freitas, C.R., Schmekal, A., 2006. Studies of corrosion/condensation process in

558 the Glowworm Cave, New Zealand. Int. J. Speleol. 35, 75–81.

559   Di Maggio, C., Madonia, G., Parise M., Vattano, M., 2012. Karst of Sicily and its

560   conservation. J. Caves Karst Stud. 74(2), 157-172.

561   Doran, L.M., Hill, C.A., 1998. Gypsum trays in Torgac cave, New Mexico. J. Caves

562   Karst Stud. 60(1), 39-43.

563   Dronkert, H., 1977. The evaporites of the Sorbas Basin. Revista de Investigación

564   Geológica de la Diputación de Barcelona, 33, 55–76.

565   Esteban-Parra, M.J., Rodrigo, F.S., Castro-Diez, Y., 1998. Spatial and temporal

566   patterns of precipitation in Spain for the period 1880–1992. Int. J. Climatol. 18,

567   1557–1574.

568   Evans, N.P., Turchyn, A., Gázquez, F., Bontognali, T.R.R., Chapman, H., Hodell, D.,

569   2015. Coupled measurements of $\delta^{18}O$ and δD of hydration water and salinity of

570   fluid inclusions in gypsum from the Messinian Yesares member, Sorbas Basin (SE

571   Spain). Earth Planet. Sci. Lett. 430, 499-510.

572   Fernández-Cortés, A., Calaforra, A., Jimenez-Espinosa, R., Sanchez-Martos, F.,

573   2006.Geostatistical spatiotemporal analysis of air temperature as an aid to

574   delineating thermal stability zones in a potential show cave: implications for

575   environmental management. J. Environ. Manage. 81, 371–383.

576   Fernández-Cortés, A., Calaforra, A., Sanchez-Martos, F., 2008. Hydrogeochemical

577   processes as environmental indicators in drip water: study of the Cueva del Agua

578   (Southern Spain). Int. J. Speleol. 37: 41-52.

579   Fontes, J.C., Gonfiantini, R., 1967. Fractionnement isotopique de l'hydrogène dans

580   l'eau de cristallistion du gypse. Cr. Acad. Sci. d. Nat. 265, 4-6.

581   Ford, D.C., Williams, P.W., 1989. Karst geomorphology and hydrology. London

582   Unwin Hyman, 601 pp.

583   Forti, P., 1996. Speleothems and cave minerals in gypsum caves. Int. J. Speleol. 25,

584   91–104.

585   Forti, P, Sauro, U., 1996. The gypsum karst of Italy. Int. J. Speleol. 25, 239–250.

586   Galve, J.P., Gutiérrez, F., Lucha, P., Guerrero, J., Bonachea, J., Remondo, J.,

587   Cendrero, A., 2008. Probabilistic sinkhole modeling for hazard assessment. Earth

588   Surf. Proc. Land. 34, 437-452.

589   Galve, J.P., Gutiérrez, F., Lucha, P., Bonachea, J., Cendrero, A., Gimeno, M.J.,

590   Gutiérrez, M., Pardo, G., Remondo, J., Sánchez, J.A., 2009. Sinkholes in the salt-

591   bearing evaporite karst of the Ebro River valley upstream of Zaragoza city (NE

592   Spain). Geomorphological mapping and analysis as a basis for risk management.

593   Geomorphology 108, 145-158.

594   Gat, J. R., 1996. Oxygen and hydrogen isotopes in the hydrologic cycle, Annu. Rev.

595   Earth Planet. Sci., 24, 225–262.

596   Gázquez, F., Calaforra, J.M., Sanna, L., Forti, P., 2011. Espeleotemas de yeso: >Un

597   nuevo proxy paleoclimático? Boletín de la Real Sociedad Española de Historia

598   Natural, 105 (1–4),15–24.

599   Gázquez, F., Calaforra, J.M., Rull, F., 2012. Boxwork and ferromanganese coatings

600   in hypogenic caves: an example from Sima de la Higuera Cave (Murcia, SE

601   Spain). Geomorphology 177-178, 158-166.

602   Gázquez, F., Calaforra, JM., Stöll, H., Sanna, L., Forti, P., Lauritzen, S-E., Delgado-

603   Huertas, A., Rull, F., Martínez-Frías, J., 2013. Isotopic and trace element

604   evolution in the Naica aquifer (Chihuahua, Mexico over the past 60.000 yrs

605   revealed by speleothems. Quart. Res. 80(3), 510–521.

606 Gázquez, F., Calaforra, J.M., 2014. The Gypsum Karst of Sorbas, Betic Chain. In:

607   Gutiérrez, F., Gutiérrez, M. (Eds.), Landscapes and Landforms of Spain. Springer,

608   pp. 127–135.

609 Gázquez, F., Calaforra, J.M., Forti, P., De Waele, J., Sanna, L., 2015a. The role of

610   condensation in the evolution of dissolutional forms in gypsum caves: study case

611   in the karst of Sorbas (SE Spain). Geomorphology 229, 100–111.

612 Gázquez, F., Calaforra, J.M., Fernández-Cortés, A., 2015b. Flash flood events

613   recorded by air temperature changes in caves: A case study in Covadura Cave

614   (SE Spain). J. Hydrol. 541, 136–145.

615   Gázquez, F., Mather, I., Rolfe, J., Evans, N.P., Herwartz, D., Staubwasser, M.

616   Hodell D.A., 2015c. Simultaneous analysis of $^{17}O/^{16}O, ^{18}O/^{16}O$ and $^{2}H/^{1}H$ of

617   gypsum hydration water by cavity ringdown laser spectroscopy. Rapid Commun.

618   Mass Spectrom. 21, 1997-2006.

619 Gázquez, F., Evans, N.P., David. A. Hodell 2017. Precise and accurate isotope

620   fractionation factors ($\alpha^{17}O$, $\alpha^{18}O$ and αD) for water and $CaSO_4 \cdot 2H_2O$ (gypsum).

621   Geochim. Cosmochim. Acta, 198, 259-270.

622 Gonfiantini, R., Fontes, J.C., 1963. Oxygen isotopic fractionation in the water of

623   crystallization of gypsum. Nature 200, 644-646.

624 Gutiérrez, F., Cooper, A.H., 2013. Surface morphology of gypsum karst. In: Frumkin

625   A (ed) Treatise on geomorphology. Karst geomorphology, vol 6. Elsevier, San

626   Diego, pp 425–437.

627 Hodell, D., Turchyn, A.V., Wiseman, C.J., Escobar, J., Curtis, J.H., Brenner, M., Gilli,

628   A. Mueller, A.D., Anselmetti, F., Aritzegui, D., Brown, E., 2012. Late Glacial

629   temperature and precipitation changes in the lowland Neotropics by tandem

measurement of $\delta^{18}O$ in biogenic carbonate and gypsum hydration water. Geochim. Cosmochim. Acta. 77, 352-368.

Horita, J., Wesolowski, D.J., 1994. Liquid–vapor fractionation of oxygen and hydrogen isotopes of water from the freezing to the critical temperature, Geochim. Cosmochim. Acta, 58, 3425–3437.

Ingraham, N.L., Matthews, R.A., 1988. Fog drip as a source of groundwater recharge in norther Kenya. Water Resour. Res. 24, 1406-1410.

Ingraham, N.L., Matthews, R.A., 1990. A stable isotopic study of fog: the Point Reyes Peninsula, California, U.S.A. Chem. Geol. 80, 281-290.

Jameson, R.A., 1991. Features of condensation corrosion in caves of the Greenbrier karst, West Virginia. Natl. Speleol. Soc. Bull. 53, 44.

Jones, P., Harris, I., 2011. Climate data provided by CRU TS 3.1 — University of East Anglia Climate Research Unit (CRU). CRU Time Series (TS) high resolution gridded datasets ([Internet]) NCAS British Atmospheric Data Centre, 2008 (accessed 15.01.13).

Klimchouk, A., Forti, P., Cooper, A., 1996. Gypsum karst of the world: a brief overview. Int. J. Speleol. 25, 159–181.

Klimchouk, A., Andrejchuk, V., 1996. Environmental problems in gypsum karst terrains. Int. J. Speleol. 5 (3-4), 145-156.

Klimchouk, A.B., Aksem, S.D., 2002. Gypsum karst in the Western Ukraine: hydrochemistry solution rates. Carbonates Evaporites 17(2),142–153.

Krijgsman, W., Fortuin, A.R., Hilgen, F.J., Sierro, F.J., 2001. Astrochronology for the Messinian Sorbas basin (SE Spain) and orbital (precessional) forcing for evaporite cyclicity. Sed. Geol., 140, 43–60.

654   Landais, A., Barkan, E., Yarik, D., Luz, B. 2006. The triple isotopic composition of
655   oxygen in leaf water, Geochim. Cosmochim. Acta, 70, 4105-4115–316

656   Luz, B., Barkan, E., Yam R., Shemesh, A. 2009. Fractionation of oxygen and
657   hydrogen isotopes in evaporating water. Geochim. Cosmochim. Acta, 73, 6697–
658   6703.

659   Luz, B., Barkan E., 2010. Variations of $^{17}O/^{16}O$ and $^{18}O/^{16}O$ in meteoric waters
660   Geochim. Cosmochim. Acta 74, 6276–6286.

661   Madonia, G., Vattano, M., 2011, New knowledge on the Monte Conca gypsum karst
662   system (central-western Sicily, Italy). Acta Carsol., 40(1), 53–64.

663   Mook W.G., 2000. Environmental Isotopes in the Hydrological Cycle: Principles and
664   Applications, Vol. I: Introduction - Theory, Methods, Review. UNESCO, IAEA,
665   Paris.

666   Sanna, L., Saez, F., Simonsen, S., Constantin, S., Calaforra, J.M., Forti, P.,
667   Lauritzen, S.E., 2010. Uranium-series dating of gypsum speleothems:
668   methodology and examples. Int. J. Speleol. 39 (1), 35–46.

669   Sanna, L., Gázquez, F., Calaforra, J.M., 2012. A geomorphological approach in the
670   study of hydrogeology of gypsum karst of Sorbas (SE Spain). Geografia Fisica e
671   Dinamica Quaternaria 35, 153–166.

672   Sarbu, S.M., Lascu, C., 1997. Condensation Corrosion in Movile Cave, Romania. J.
673   Caves Karst Stud. 59, 99–102.

674   Sofer, Z., 1978. Isotopic composition of hydration water in gypsum. Geochim.
675   Cosmochim. Acta 42, 1141-1149.

676   Steig, E.J., Gkinis, V., Schauer, A.J., Schoenemann, S.W., Samek, K., Hoffnagle, J.,
677   Dennis, K.J., Tan S.M., 2014. Calibrated high-precision ^{17}O-excess

678   measurements using laser-current tuned cavity ring-down spectroscopy*, Atmos.*

679   *Meas. Tech.* 7, 2421-2435.

680   Surma, J., Assonov, S., Bolourchi, M.J., Staubwasser, M., 2015. Triple oxygen

681   isotope signatures in evaporated water bodies from the Sistan Oasis, Iran,

682   Geophys. Res. Lett. 42, 8456–8462.

683   Tarhule-Lips, R.F.A., Ford, D.C., 1998. Condensation corrosion in caves on Cayman

684   Brac and Isla de Mona. J. Caves Karst Stud. 60, 84–95.

685   Wigley, TML. 1973. Chemical evolution of the system calcite-gypsum-water.

686   Canadian J. Earth Sci. 10(2), 306-315.

687

688   **FIGURE CAPTIONS**

689   **Figure 1. a.** Geological setting and panoramic view of the gypsum karst of Sorbas.

690   Speleothems in the caves include: I) Upper Bosque Gallery: **b.** Gypsum popcorn; **c.**

691   Gypsum popcorn and veins; II) Nieves Gallery: **d.** Gypsum stalactites; **e.** Gypsum

692   coralloids; III) Lower Bosque Gallery: **f.** Hollow gypsum stalagmites; IV) Sima Fe: **g.**

693   Gypsum "Christmas tree"; V) C3 Cave: **h.** Gypsum rim crust; **i.** Gypsum needles

694   within clayey sediments; VI) El Peral-Majadas Viejas Quarry: **j.** Gypsum flowstone on

695   speleothemic calcite.

696

697   **Figure 2.** Schematic section of the upper levels of Covadura Cave: Upper and Lower

698   Bosque Galleries and Nieves Gallery. Ibutton[®] sensors (see supplementary material)

699   monitored temperature and humidity in locations S1 and S3 and temperature in

700   location S2. The vertical bar to the left shows the depth of interbedded gypsum (G)

701   and marl (M) strata. Condensation water was sampled using a bespoke

condensation collector placed in the Lower Bosque Gallery, represented by the red circle (C). Espeleoclub Almería is credited for the topographic maps of the cave (Ayuso et al., 2014).

Figure 3. $\delta^{18}O$ vs δD (V-SMOW) of waters that formed gypsum speleothems, inferred from GHW after correction with fractionation factors (see main text). Speleothems generated from significant amounts of condensation water lie on an evaporation line whose origin matches the isotopic composition of dripwater in these caves. Speleothems precipitated from infiltration water match the isotopic composition of fast discharge-infiltration in the caves after intense rain events, similar to the mean of rainwater and the springs in the Sorbas karst.

Figure 4. Effective condensation rate (condensation – evaporation) in the Lower Bosque Gallery and rainfall amount in the Sorbas area during the period of study. The isotopic compositions of water samples are given.

Figure 5. Microclimate parameters monitored in the upper levels of Covadura Cave and in the external atmosphere. **(a)** Air temperature; **(b)** Air relative humidity; **(c)** Condensation rate in Lower Bosque Gallery, recovered using an in-house condensation collector.

723   **Figure 6**. Schematic diagram of air mass exchange in the upper levels of Covadura

724   Cave and its implications for condensation mechanisms and gypsum speleothem

725   formation. **(a)** Colder (denser) air accumulates in the cave relative to warmer (lighter)

726   air outside. In this situation, exchange of external and internal air is limited and water

727   condenses on the cave walls and ceiling, resulting in dissolution of gypsum between

728   June and December. **(b)** Decrease of the external air temperature during winter

729   favors exchange of cave air with external air. Colder (generally drier) air gives rise to

730   intense evaporation and gypsum speleothem precipitation occurs between January

731   and May.

732

733   **Figure 7.** $\delta^{18}O$ and electrical conductivity of waters (condensation, dripwater and

734   infiltration water). The dripwater shows intermediate values of $\delta^{18}O$ and conductivity,

735   which suggests mixing of condensation and infiltration water.

736

737   **Figure 8.** Cross-plots of **(a)** d-excess and **(b)** $\Delta^{17}O$ vs $\delta^{18}O$ of mother water that

738   formed the gypsum speleothems considered in this study. The isotopic composition

739   of the rainwater, condensation water and dripwater in the cave are also given.

740

741   **Figure 9.** Isotopic mass balance modelling of hydration water of gypsum

742   speleothems corrected for fractionation. $\Delta^{17}O$ vs $\delta^{18}O$ and d-excess vs $\delta^{18}O$ during

743   evaporation of waters with different initial isotopic compositions: condensation water

744   ($\delta^{17}O$ =-1.4‰; $\delta^{18}O$= of -2.7‰; δD = -11.4‰; d-excess=10.2‰; $\Delta^{17}O$ = 19 per meg),

745   infiltration water (springs) ($\delta^{17}O$ =-2.7‰; $\delta^{18}O$= of -5.2‰; δD = -31.9‰; d-excess=

746   9.9‰; $\Delta^{17}O$ = 15 per meg) and dripwater ($\delta^{17}O$ =-2.0‰; $\delta^{18}O$= -3.8‰; δD = -16.9‰;

747   d-excess=13.4‰; $\Delta^{17}O$ = 17 per meg). Evaporation trajectories were modelled at

748   15°C (mean cave air temperature) for different conditions or relative humidity.

749   Isotopic equilibrium between the solution and the air vapour is assumed, as well as

750   isotopic diffusion and absence of turbulence during the evaporation process (i.e. no

751   wind). The model considers different ratios of evaporation and outflow (water film

752   migration) (X_E), where X_E=0 means no evaporation, and X_E=1 means a non-dripping

753   speleothem, where all water is lost via evaporation.

Figure 1
[Click here to download high resolution image](#)

Figure 1. (a) Panoramic view and location maps of the study area (Spain). (b, c) gypsum popcorn and veins. (d) gypsum stalactites. (e) gypsum coralloids (3 cm). (f) (5 cm). (g) (20 cm). (h) gypsum hostrock, gypsum crust. (i) gypsum needles (2 cm). (j) gypsum flowstone, calcite flowstone, gypsum hostrock.
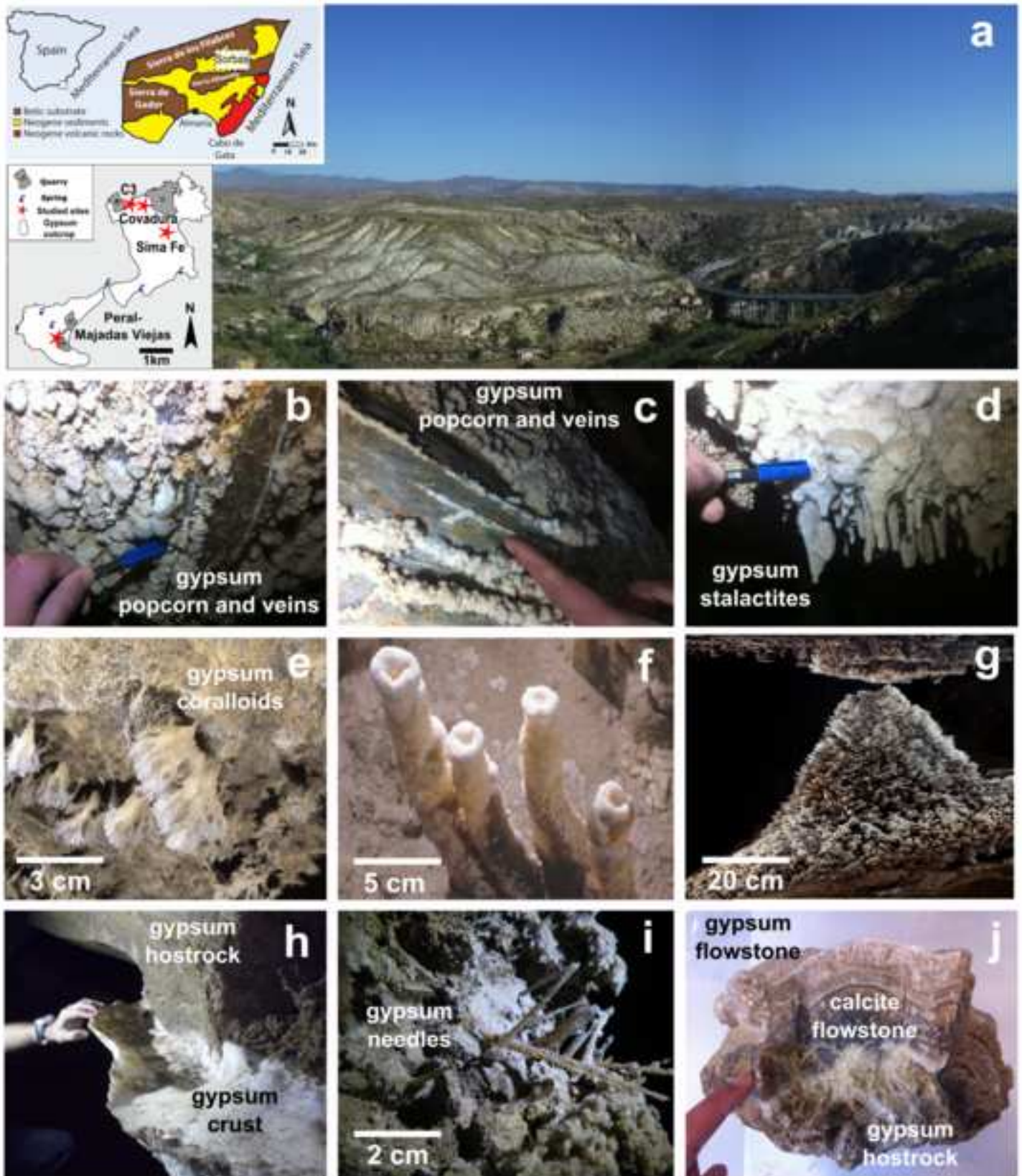
Figure 2
Click here to download high resolution image

COVADURA CAVE (BOSQUE BRANCH)
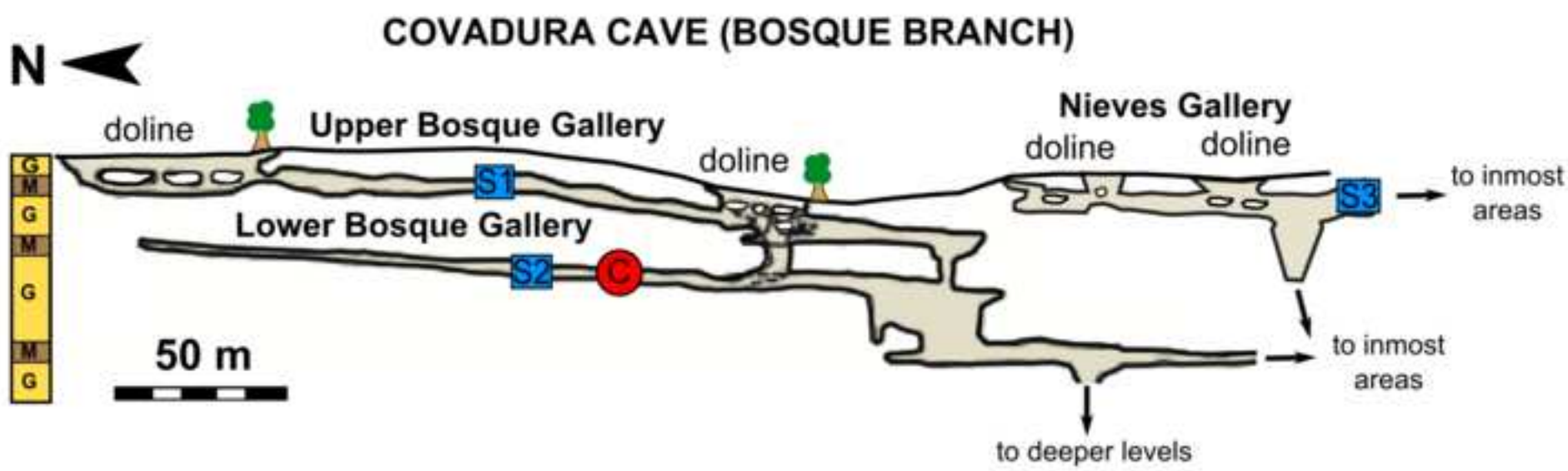
Figure 3
Click here to download high resolution image
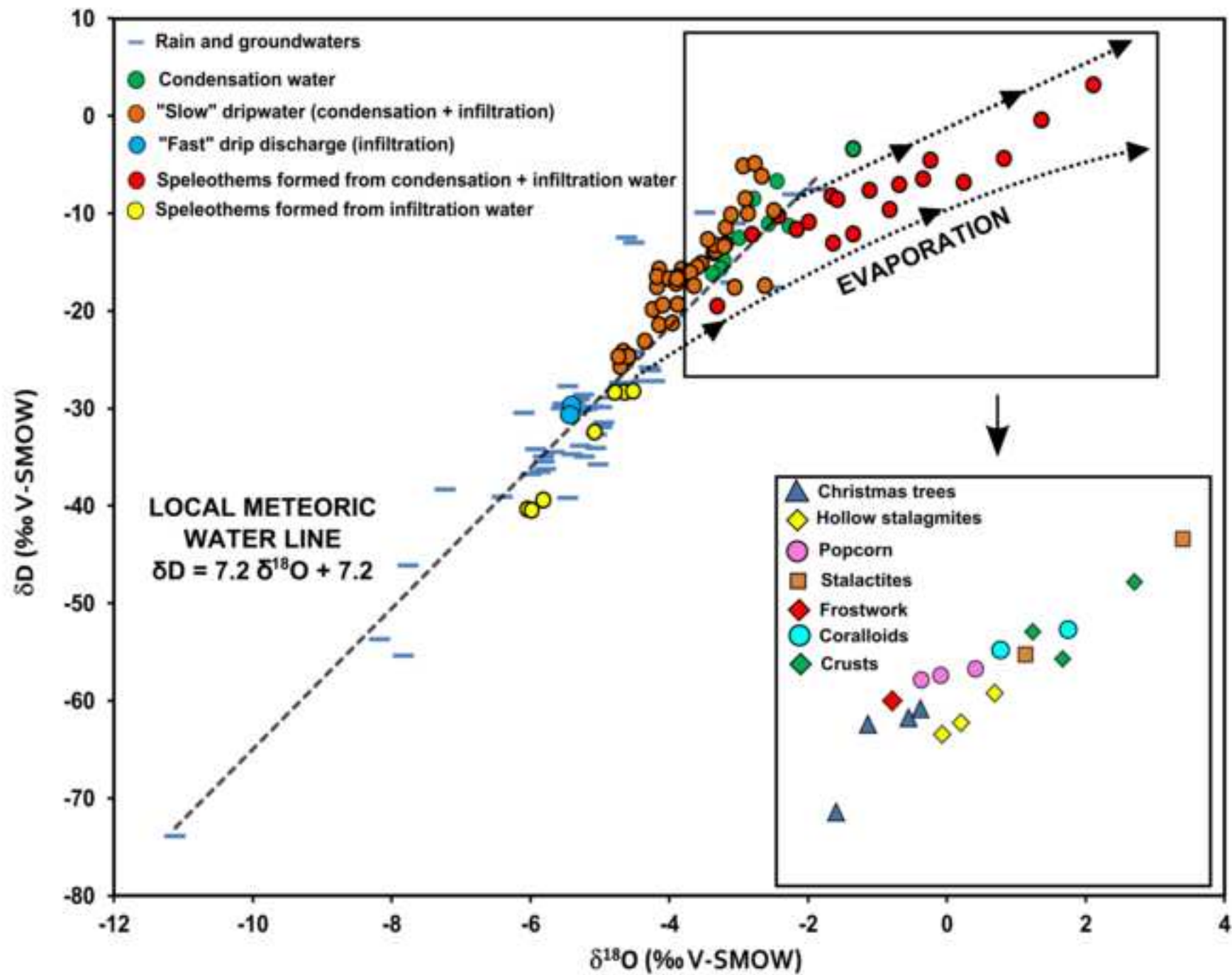
Figure 4
Click here to download high resolution image
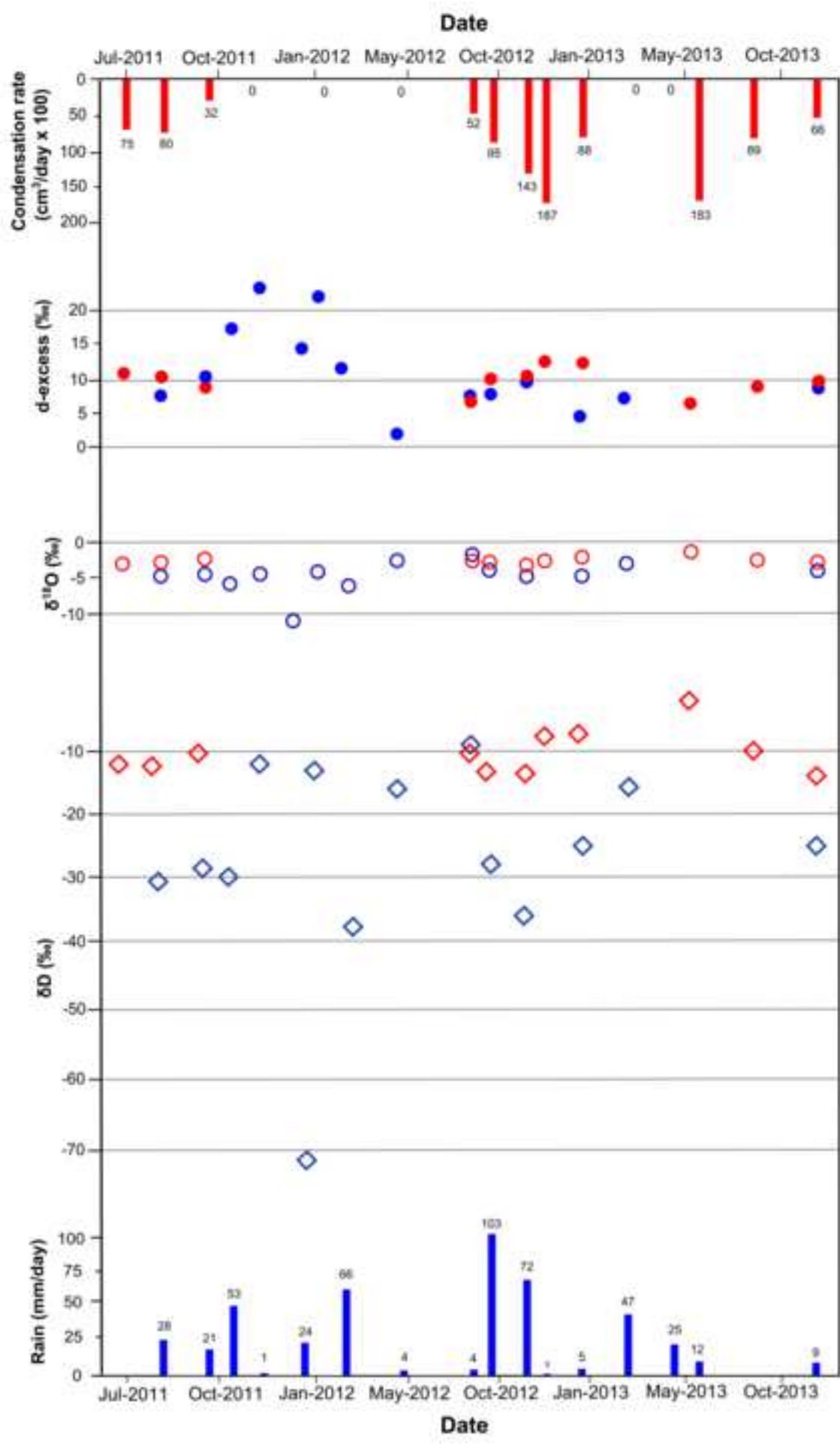
Figure 5
Click here to download high resolution image
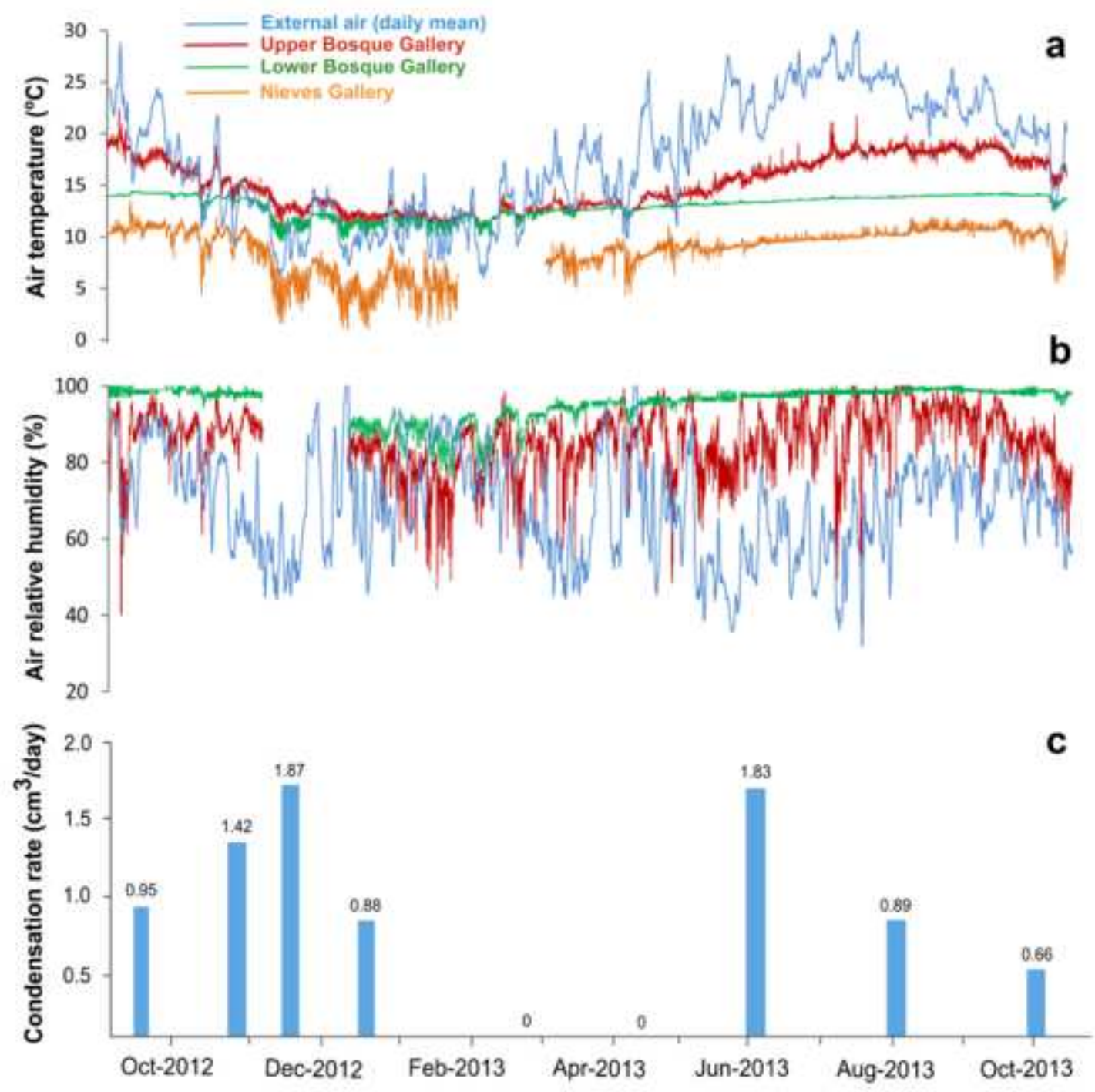
a **Warmer air** — June - December
~15-35 °C
Gypsum hostrock
Limited air exchange
Condensation and gypsum dissolution
~10-18 °C
RH=100%

b **Colder air** — January-May
~5-15 °C
Gypsum hostrock
Intense air exchange
Evaporation and gypsum precipitation
~4-15 °C
RH=75-85%
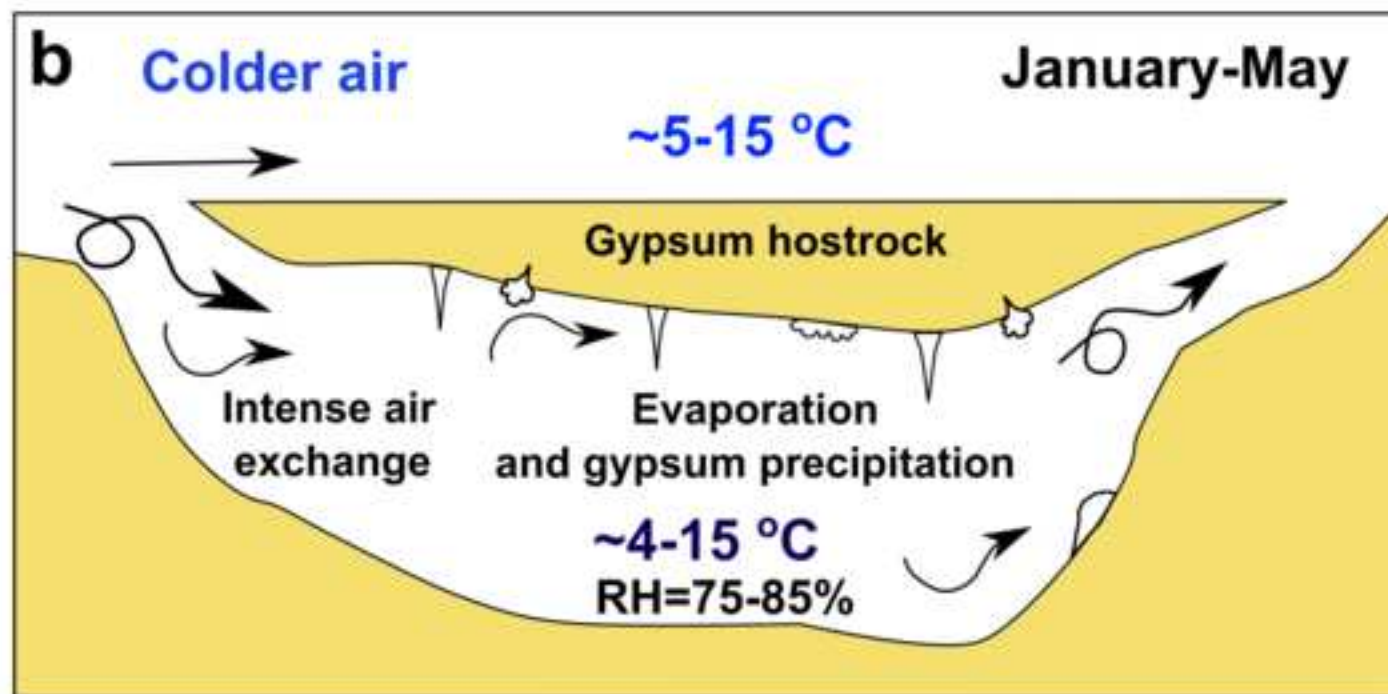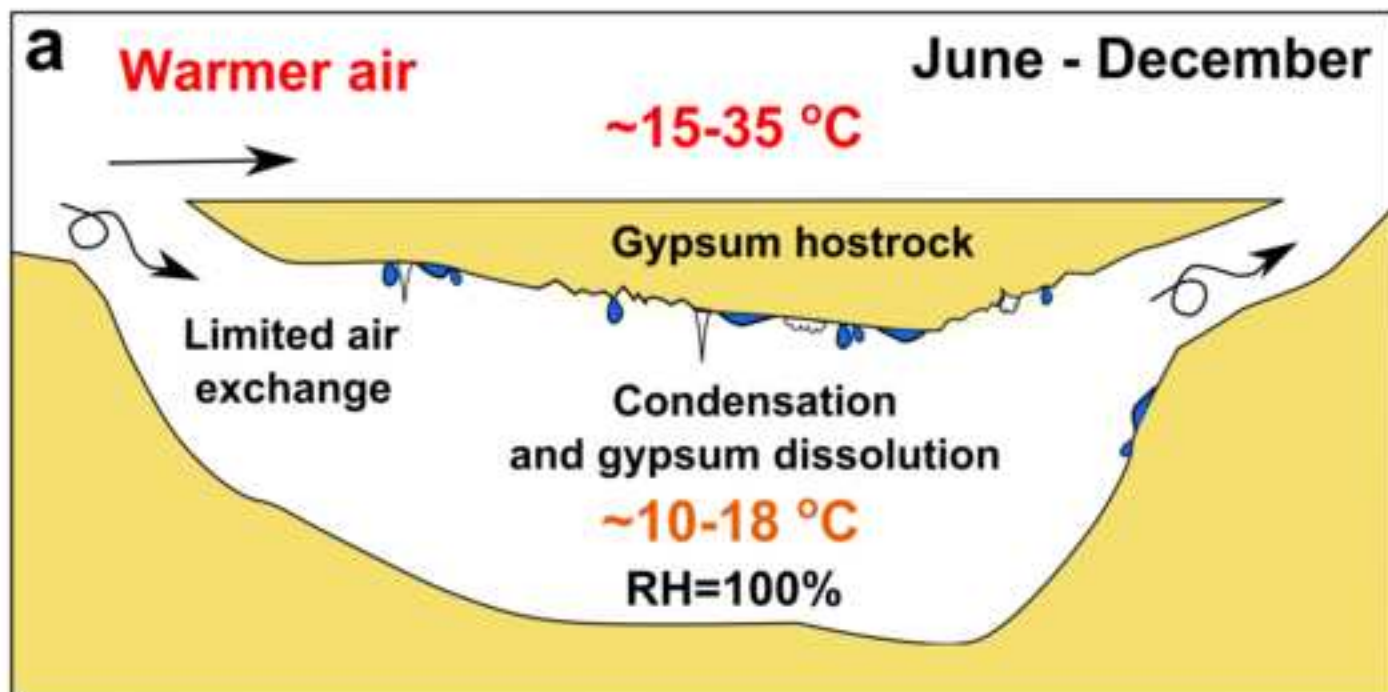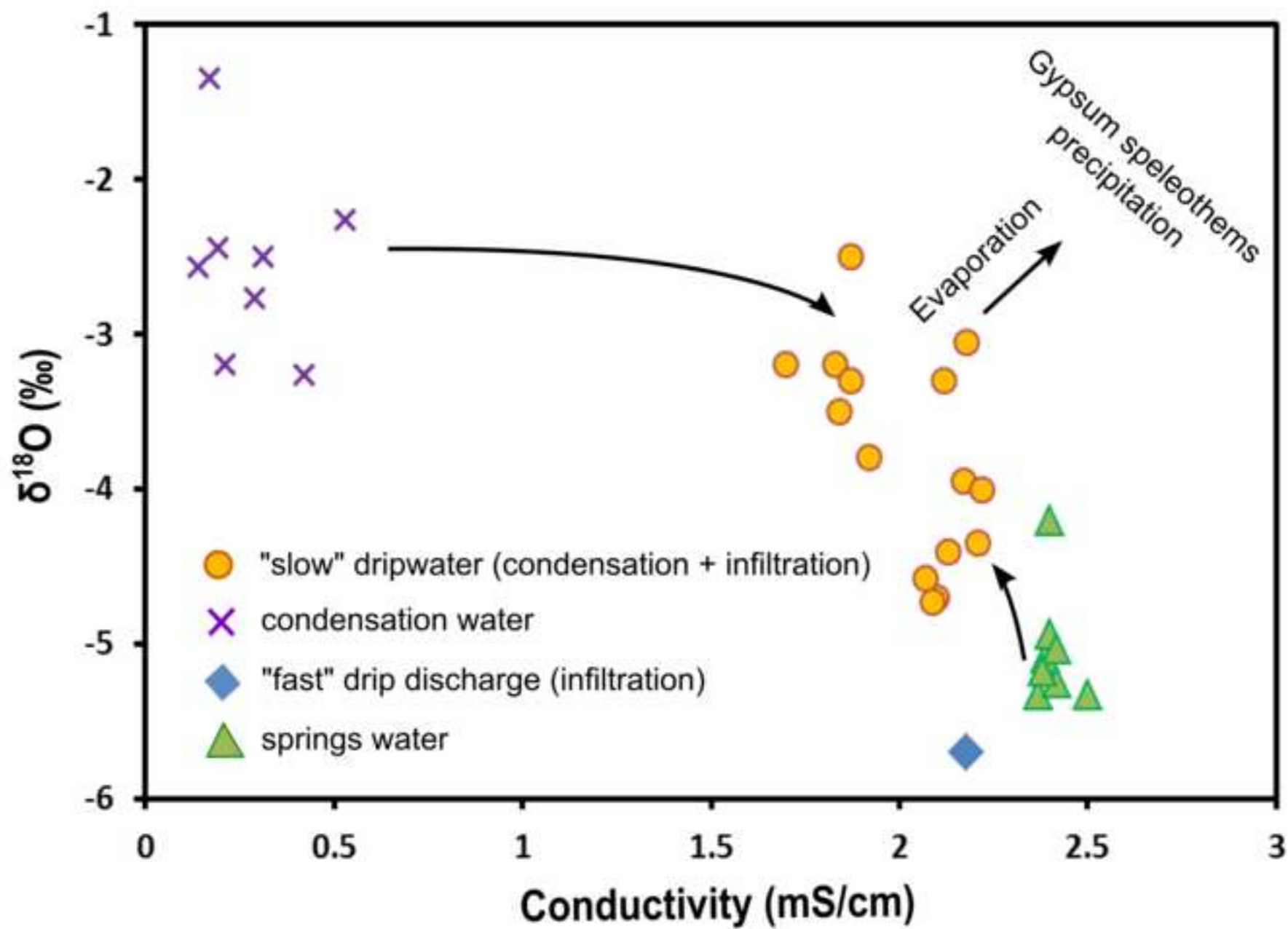
Figure 8
Click here to download high resolution image

a
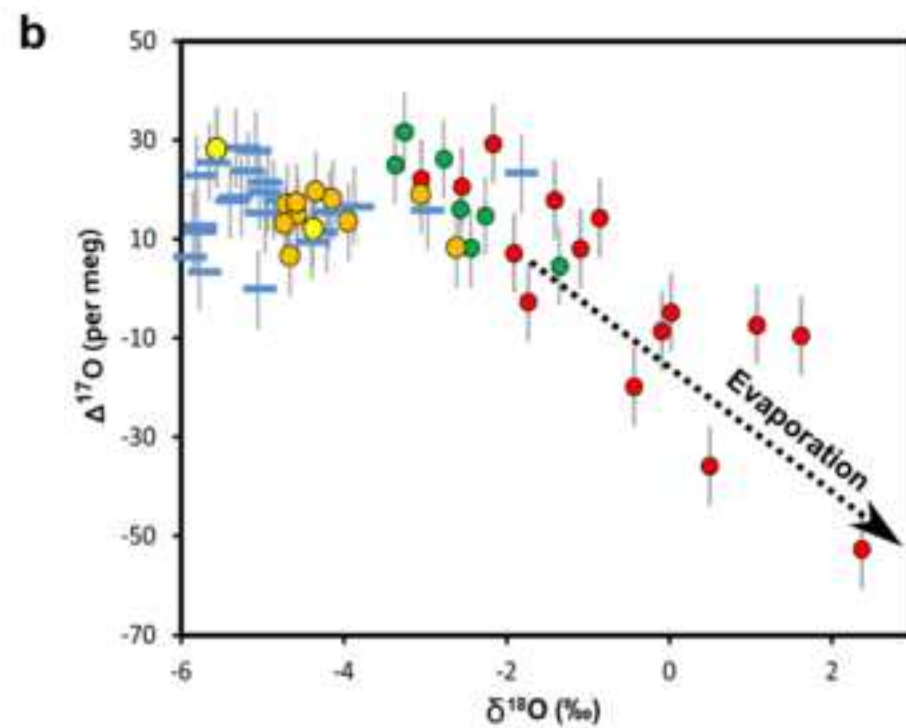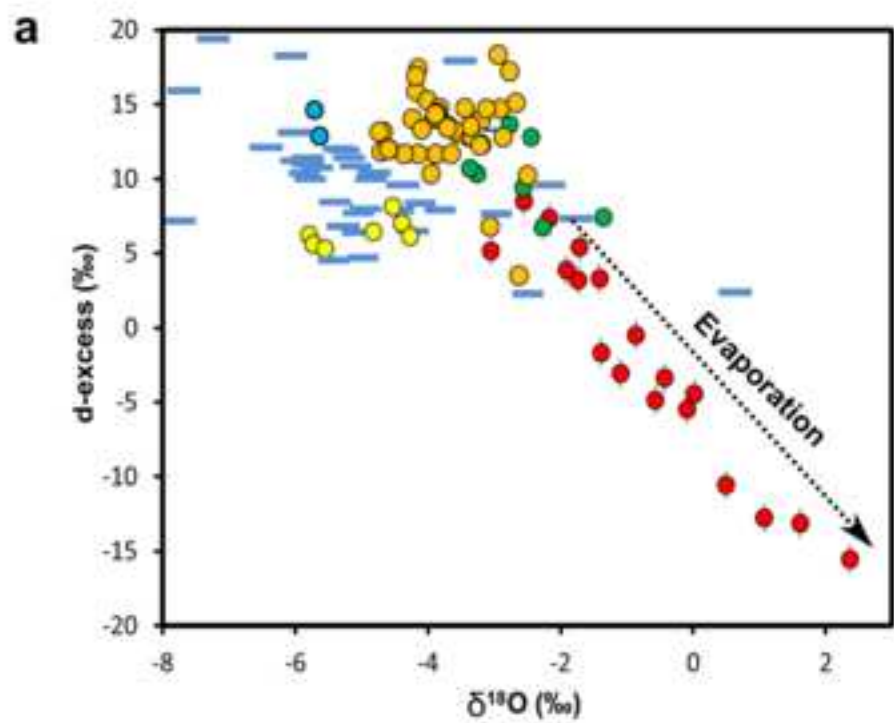
- Rain and groundwaters
- Condensation water
- "Slow" dripwater (condensation + infiltration)
- "Fast" drip discharge (infiltration)

b

- Speleothems formed from condensation + infiltration water
- Speleothems formed from infiltration water

evaporation trajectories
— condensation water   — infiltration water   — dripwater (condensation + infiltration)

● speleothems formed from evaporation of dripwater (condensation + infiltration)
● speleothems formed from inflitration water
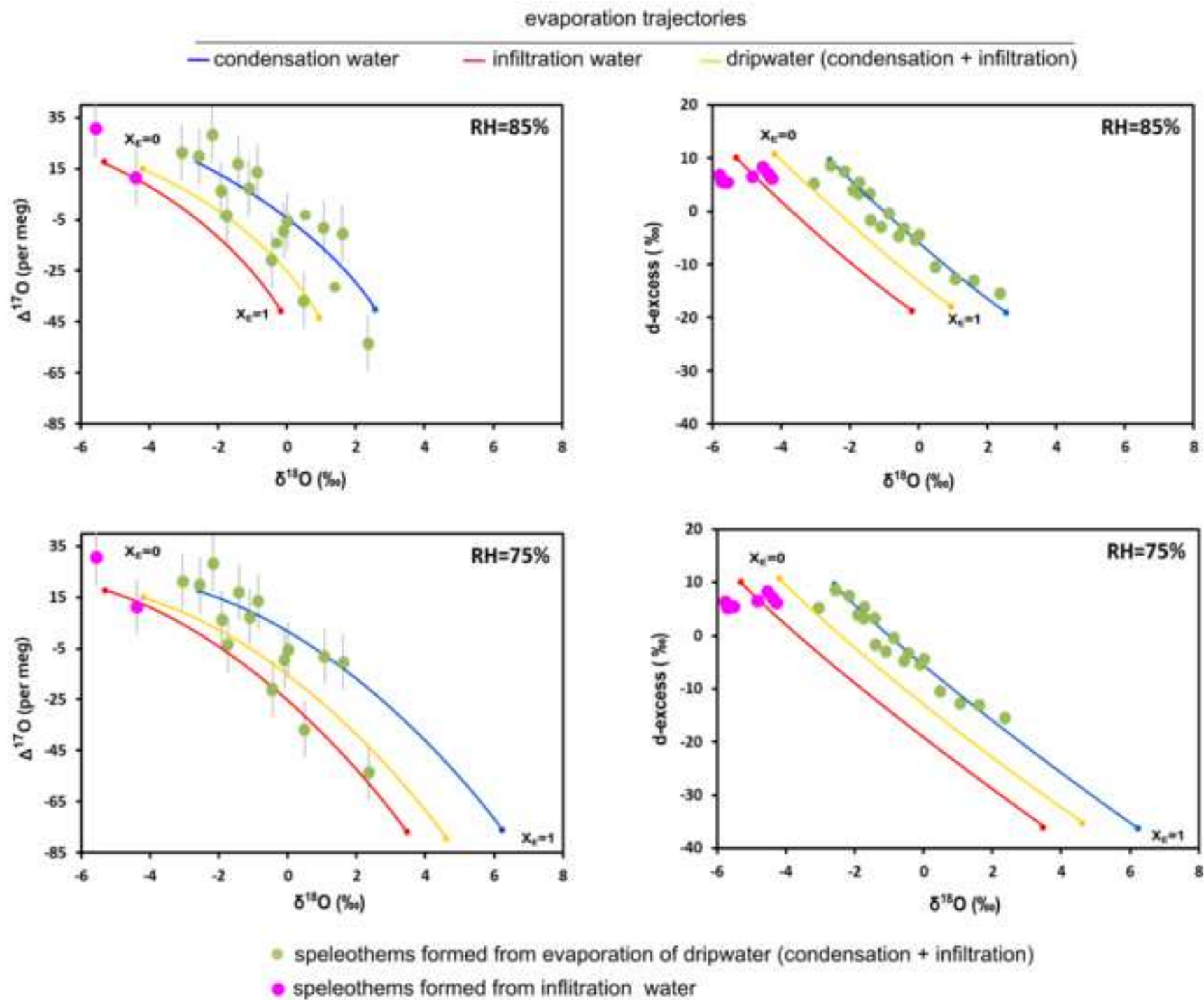
Table 1

Sample ID	Description	Cave	$\delta^{17}O_{ghw}$ (‰)	1σ	$\delta^{18}O_{ghw}$ (‰)	1σ	δD_{ghw} (‰)	1σ	$\delta^{17}O_{mw}$ (‰)	$\delta^{18}O_{mw}$ (‰)	δD_{mw} (‰)	d-excess mw (‰)	1σ	$\Delta^{17}O$ mw (per meg)	1σ	H_2O (%)
NIEVES-01	Popcorn on the cave ceiling	Nieves Cave	1.63	0.03	3.12	0.03	-26.95	0.17	-0.25	-0.44	-6.79	-3.3	0.2	-21	15	20.3
NIEVES-02	Frostwork on the cave ceiling	Nieves Cave	0.76	0.02	1.37	0.02	-30.10	0.31	-1.12	-2.17	-10.00	7.3	0.3	28	8	20.9
NIEVES-03	Crust detached from the cave ceiling	Nieves Cave	2.10	0.02	4.05	0.03	-26.72	0.13	0.22	0.49	-6.56	-10.5	0.2	-37	12	20.5
NIEVES-04	Stalactite	Nieves Cave	3.08	0.02	5.93	0.03	-16.93	0.25	1.19	2.36	3.44	-15.5	0.1	-53	11	19.9
NIEVES-05	Popcorn on cave ceiling	Nieves Cave	2.44	0.03	4.63	0.03	-24.32	0.15	0.56	1.07	-4.11	-12.7	0.4	-8	17	20.7
NIEVES-06	Coralloids on cave ceiling	Nieves Cave	1.44	0.02	2.69	0.02	-27.54	0.08	-0.44	-0.86	-7.39	-0.5	0.3	13	21	20.8
NIEVES-07	Detached stalactite	Nieves Cave	1.82	0.02	3.46	0.04	-26.35	0.26	-0.06	-0.09	-6.18	-5.5	0.2	-9	8	20.9
BOS-UP-01	Crust on cave ceiling	Up. Bosque	2.72	0.03	5.17	0.05	-20.46	0.32	0.84	1.61	-0.16	-13.1	0.1	-10	17	20.8
BOS-UP-02	Popcorn on cave ceiling	Up. Bosque	1.15	0.02	2.14	0.03	-28.09	-0.73	-1.41	-1.66	-8.25	5.0	0.4	17	12	20.6
BOS-UP-03	Crust on cave ceiling	Up. Bosque	1.88	0.03	3.57	0.04	-24.49	0.22	0.00	0.02	-4.28	-4.4	0.4	-6	10	20.5
BOS-LOW-01	Hollow stalagmite	Low. Bosque	1.31	0.01	2.45	0.02	-31.89	0.14	-0.57	-1.10	-11.83	-3.0	0.1	8	9	20.0
BOS-LOW-02	Hollow stalagmite	Low. Bosque	n.a	n.a	2.98	0.05	-29.48	0.24	n.a	-0.57	-9.38	-4.8	0.5	n.a		20.6
BOS-LOW-03	Hollow stalagmite	Low. Bosque	n.a	n.a	2.16	0.03	-32.83	0.36	n.a	-1.39	-12.79	0.0	0.6	n.a		20.9
C3-01	Needles in clayey sediment	C3 Cave	-0.43	0.04	-0.85	0.04	-47.85	0.36	-2.31	-4.39	-28.12	7.0	0.2	11	10	20.1
C3-02	Needles in clayey sediment	C3 Cave	n.a	n.a	-0.99	0.07	-47.80	0.36	n.a	-4.53	-28.07	8.2	0.4	n.a		19.9
C3-03	Needles in clayey sediment	C3 Cave	n.a	n.a	-0.73	0.02	-47.73	0.34	n.a	-4.27	-28.00	7.8	0.5	n.a		20.0
C3-04	Needles in clayey sediment	C3 Cave	n.a	n.a	-1.29	0.03	-51.81	0.15	n.a	-4.83	-32.16	8.1	0.4	n.a		19.9
C3-05	Popcorn on cave ceiling	C3 Cave	n.a	n.a	1.84	0.02	-28.41	0.10	n.a	-1.71	-8.28	5.4	0.4	n.a		20.1
FE-BL-UP	Gypsum tray above "tree"	Sima Fe Cave	0.55	0.03	0.99	0.03	-31.99	0.28	-1.33	-2.56	-11.93	8.5	0.2	20	13	20.5
FE-BL-BOTT	Gypsum "tree"	Sima Fe Cave	0.29	0.03	0.49	0.03	-39.13	0.18	-1.59	-3.05	-19.22	5.2	0.3	21	18	20.4
FE-RJ-UP	Gypsum tray aboce "tree"	Sima Fe Cave	0.96	0.02	1.81	0.05	-30.74	0.29	-0.92	-1.74	-10.65	3.2	0.2	-4	11	20.5
FE-RJ-BOTT	Gypsum "tree"	Sima Fe Cave	0.87	0.04	1.63	0.05	-31.47	0.21	-1.01	-1.92	-11.40	3.9	0.1	7	14	20.5
MJ-05-01	Flowstone Upper part	Peral quarry	-1.04	0.03	-2.03	0.03	-58.68	0.30	-2.91	-5.56	-39.18	5.3	0.2	30	16	20.1
MJ-05-02	Flowstone Lower part	Peral quarry	n.a	n.a	-2.26	0.05	-59.58	0.18	n.a	-5.80	-40.09	6.2	0.4	n.a		19.9
MJ-05-03	Flowstone Upper part	Peral quarry	n.a	n.a	-2.20	0.03	-59.67	0.32	n.a	-5.73	-40.18	5.6	0.5	n.a		20.3

Table 1

Table 2

Sample ID	Type	Date	$\delta^{17}O$ (‰)	1σ	$\delta^{18}O$ (‰)	1σ	δD (‰)	1σ	d-excess (‰)	$\Delta^{17}O$ (per meg)	Conductivity (mS/cm)
RAIN-01	Rain	02/10/2009	n.a		-5.9	<0.3	-34.2	<2	13.1	n.a	n.a
RAIN-02	Rain	18/01/2010	n.a		-7.8	<0.3	-55.4	<2	7.2	n.a	n.a
RAIN-03	Rain	16/03/2010	n.a		-8.2	<0.3	-53.7	<2	11.6	n.a	n.a
RAIN-04	Rain	28/04/2010	n.a		-5.5	<0.3	-39.2	<2	4.5	n.a	n.a
RAIN-05	Rain	03/06/2010	n.a		-4.5	<0.3	-24.2	<2	11.8	n.a	n.a
RAIN-06	Rain	20/07/2010	n.a		-5.2	<0.3	-35.0	<2	6.8	n.a	n.a
RAIN-07	Rain	06/09/2010	n.a		-2.2	<0.3	-8.1	<2	9.7	n.a	n.a
RAIN-08	Rain	19/11/2010	n.a		-4.4	<0.3	-27.2	<2	7.9	n.a	n.a
RAIN-09	Rain	24/01/2011	n.a		-7.2	<0.3	-38.4	<2	19.4	n.a	n.a
RAIN-10	Rain	26/02/2011	n.a		-7.8	<0.3	-46.2	<2	15.9	n.a	n.a
RAIN-11	Rain	07/04/2011	n.a		-3.5	<0.3	-9.9	<2	18.0	n.a	n.a
RAIN-12	Rain	03/05/2011	n.a		-5.3	<0.3	-33.9	<2	8.3	n.a	n.a
RAIN-13	Rain	09/06/2011	n.a		-3.0	<0.3	-11.1	<2	13.3	n.a	n.a
RAIN-14	Rain	13/09/2011	n.a		-5.0	<0.3	-31.9	<2	7.8	n.a	n.a
RAIN-15	Rain	06/11/2011	n.a		-4.7	<0.3	-27.4	<2	10.3	n.a	n.a
RAIN-16	Rain	06/12/2011	n.a		-6.1	<0.3	-30.5	<2	18.3	n.a	n.a
RAIN-17	Rain	11/01/2012	n.a		-4.6	<0.3	-12.5	<2	24.3	n.a	n.a
RAIN-18	Rain	01/03/2012	n.a		-11.1	<0.3	-73.9	<2	15.0	n.a	n.a
RAIN-19	Rain	18/09/2012	-0.94	0.02	-1.81	0.02	-7.09	0.12	6.8	23	n.a
RAIN-20	Rain	11/10/2012	-2.19	0.03	-4.18	0.04	-25.10	0.08	10.3	16	n.a
RAIN-21	Rain	23/11/2012	-2.59	0.02	-4.93	0.02	-29.17	0.15	13.6	21	n.a
RAIN-22	Rain	28/01/2013	-2.61	0.03	-4.97	0.04	-35.07	0.21	12.8	15	n.a
RAIN-23	Rain	25/03/2013	-1.55	0.02	-2.96	0.03	-16.10	0.15	7.4	16	n.a
RAIN-24	Rain	06/11/2013	-2.32	0.03	-4.40	0.05	-25.59	0.07	9.4	10	n.a
		AVG ± 1SD	**-2.0**	**±0.7**	**-5.2**	**±2.1**	**-30.5**	**±16.1**	**11.8±4.8**	**17±5**	**n.a**
MOLINOS-01	Spring	01/03/2012	-3.08	0.03	-5.86	0.04	-36.54	0.41	10.4	14	3.29
MOLINOS-02	Spring	18/03/2012	-3.05	0.02	-5.77	0.02	-36.27	0.16	10.0	12	3.18
MOLINOS-03	Spring	24/03/2012	-2.67	0.03	-5.06	0.03	-34.10	0.16	6.4	16	n.a
MOLINOS-04	Spring	07/04/2012	-3.06	0.02	-5.80	0.01	-35.49	0.10	10.9	14	n.a
MOLINOS-05	Spring	10/08/2012	-2.84	0.02	-5.40	0.02	-34.74	0.12	8.5	16	n.a
APAS-01	Spring	11/05/2011	-2.21	0.04	-4.21	0.03	-27.21	0.15	6.5	17	2.40
APAS-02	Spring	10/08/2011	-2.66	0.02	-5.09	0.02	-29.84	0.09	10.8	11	2.39
APAS-03	Spring	01/03/2012	-2.79	0.02	-5.33	0.02	-30.59	0.22	12.0	16	2.37
APAS-04	Spring	06/06/2012	-2.76	0.03	-5.26	0.03	-30.17	0.16	11.9	18	n.a
PERAL-01	Spring	11/05/2011	-2.59	0.02	-4.94	0.03	-31.46	0.21	8.0	16	2.40
PERAL-02	Spring	01/03/2012	-2.79	0.02	-5.33	0.02	-30.59	0.22	12.0	16	2.50
PERAL-03	Spring	06/06/2012	-2.76	0.03	-5.26	0.03	-30.17	0.16	11.9	18	2.42
PERAL-04	Spring	10/08/2011	-2.65	0.03	-5.04	0.03	-32.70	0.32	7.7	16	2.42
VINICA-01	Spring	01/03/2012	-2.72	0.02	-5.18	0.04	-30.09	0.31	11.4	10	2.38
VINICA-02	Spring	01/04/2012	-2.55	0.03	-4.86	0.02	-28.91	0.13	10.0	21	n.a
		AVG ± 1SD	**-2.7**	**±0.2**	**-5.2**	**±0.4**	**-31.9**	**±2.9**	**9.9±2**	**15±3**	**2.6±0.3**

Table 2

Table 3

Sample ID	Type	Date	$\delta^{17}O$ (‰)	1σ	$\delta^{18}O$ (‰)	1σ	δD (‰)	1σ	d-excess (‰)	$\Delta^{17}O$ (per meg)	Conductivity (mS/cm)	Amount (ml/day)
CON-01	Condensation	29/07/2011	n.a		-3.0	<0.3	-12.5	<2	11.4	n.a	n.a	0.75
CON-02	Condensation	13/09/2011	n.a		-3.2	<0.3	-14.9	<2	10.7	n.a	0.21	0.80
CON-03	Condensation	06/11/2011	n.a		-2.5	<0.3	-10.4	<2	9.3	n.a	0.31	0.32
CON-04	Condensation	18/09/2012	-1.18	0.03	-2.26	0.03	-11.35	0.17	6.8	15	0.53	0.52
CON-05	Condensation	23/11/2012	-1.69	0.05	-3.26	0.06	-15.72	0.12	10.3	32	0.42	0.95
CON-06	Condensation	17/12/2012	-1.44	0.01	-2.77	0.02	-8.55	0.20	13.6	26	0.29	1.43
CON-07	Condensation	28/01/2013	-1.28	0.02	-2.44	0.02	-6.74	0.14	12.8	8	0.19	1.88
CON-08	Condensation	19/06/2013	-0.71	0.02	-1.35	0.04	-3.38	0.13	7.4	5	0.17	0.88
CON-09	Condensation	28/08/2013	-1.34	0.02	-2.57	0.04	-11.10	0.09	9.4	16	0.14	1.83
CON-10	Condensation	11/10/2013	-1.76	0.02	-3.37	0.05	-16.25	0.14	10.7	25	n.a	0.89
CON-11	Condensation	06/11/2013	-1.58	0.02	-3.04	0.05	-15.02	0.15	9.3	26	n.a	0.66
		AVG ± 1SD	**-1.4**	**±0.3**	**-2.7**	**±0.6**	**-11.4**	**±4.0**	**10.2±2**	**19±10**	**1±0.5**	**0.3± 0.1**
COV-01-01	Dripwater	18/01/2010	n.a		-4.2	<0.3	-17.6	<2	15.8	n.a	n.a	0.26
COV-01-02	Dripwater	16/03/2010	n.a		-4.1	<0.3	-15.8	<2	17.3	n.a	n.a	1.10
COV-01-03	Dripwater	28/04/2010	n.a		-4.2	<0.3	-16.5	<2	16.8	n.a	n.a	4.08
COV-01-04	Dripwater	03/06/2010	n.a		-4.0	<0.3	-16.7	<2	15.2	n.a	n.a	7.14
COV-01-05	Dripwater	20/07/2010	n.a		-3.9	<0.3	-17.2	<2	14.0	n.a	n.a	12.22
COV-01-06	Dripwater	06/09/2010	n.a		-3.9	<0.3	-19.3	<2	11.6	n.a	n.a	2.62
COV-01-07	Dripwater	19/11/2010	n.a		-3.4	<0.3	-14.1	<2	12.8	n.a	n.a	1.40
COV-01-08	Dripwater	24/01/2011	n.a		-2.9	<0.3	-5.2	<2	18.3	n.a	n.a	0.81
COV-01-09	Dripwater	26/02/2011	n.a		-2.8	<0.3	-4.9	<2	17.1	n.a	n.a	1.33
COV-01-10	Dripwater	03/05/2011	n.a		-2.9	<0.3	-8.5	<2	14.7	n.a	n.a	3.70
COV-01-11	Dripwater	01/07/2011	n.a		-3.2	<0.3	-11.5	<2	14.0	n.a	1.70	3.38
COV-01-12	Dripwater	29/07/2011	n.a		-3.2	<0.3	-13.2	<2	12.2	n.a	1.83	3.57
COV-01-13	Dripwater	13/09/2011	n.a		-3.5	<0.3	-15.2	<2	13.0	n.a	1.84	2.68
COV-01-14	Dripwater	06/11/2011	n.a		-3.8	<0.3	-16.4	<2	14.0	n.a	1.92	2.09
COV-01-15	Dripwater	06/12/2011	n.a		-3.3	<0.3	-13.9	<2	12.7	n.a	1.87	1.00
COV-01-16	Dripwater	11/01/2012	n.a		-2.5	<0.3	-9.7	<2	10.2	n.a	1.87	4.17
COV-01-17	Dripwater	01/03/2012	n.a		-3.3	<0.3	-13.2	<2	13.5	n.a	2.12	5.10
COV-01-18	Dripwater	18/04/2012	n.a		-3.4	<0.3	-12.8	<2	14.7	n.a	n.a	5.21
COV-01-19	Dripwater	26/06/2012	n.a		-4.2	<0.3	-19.9	<2	14.0	n.a	n.a	3.67
COV-01-20	Dripwater	26/07/2012	-2.17	0.03	-4.14	0.04	-21.49	0.10	11.6	18	n.a	8.33
COV-01-21	Dripwater	26/08/2012	-1.59	0.02	-3.05	0.03	-17.63	0.20	6.8	19	2.18	4.72
COV-01-22	Dripwater	19/09/2012	-2.07	0.03	-3.95	0.03	-21.26	0.10	10.3	14	2.17	11.36
COV-01-23	Dripwater	11/10/2012	-2.28	0.02	-4.35	0.03	-23.16	0.17	11.6	20	2.21	5.95
COV-01-24	Dripwater	23/11/2012	-2.47	0.02	-4.70	0.03	-25.80	0.23	11.8	17	2.10	10.41
COV-01-25	Dripwater	17/12/2012	-2.41	0.00	-4.58	0.03	-24.71	0.28	12.0	17	2.07	5.95
COV-01-26	Dripwater	28/01/2013	-2.49	0.03	-4.73	0.03	-24.71	0.10	13.1	13	2.09	4.17
COV-01-27	Dripwater	25/03/2013	-2.31	0.01	-4.41	0.04	-24.61	0.34	10.6	21	2.13	4.90
COV-01-28	Dripwater	19/06/2013	-2.10	0.03	-4.01	0.04	-22.41	0.24	9.7	16	2.22	8.33
COV-02-01	Dripwater	29/07/2011	n.a		-3.8	<0.3	-15.8	<2	14.7	n.a	n.a	n.a
COV-02-02	Dripwater	13/09/2011	n.a		-3.7	<0.3	-16.0	<2	13.5	n.a	2.16	n.a
COV-02-03	Dripwater	06/11/2011	n.a		-3.9	<0.3	-16.5	<2	14.4	n.a	2.11	n.a
COV-02-04	Dripwater	11/01/2012	n.a		-3.2	<0.3	-13.5	<2	12.2	n.a	2.07	n.a
COV-02-05	Dripwater	01/03/2012	n.a		-3.1	<0.3	-10.2	<2	14.7	n.a	2.05	n.a
COV-02-06	Dripwater	18/04/2012	n.a		-2.7	<0.3	-6.2	<2	15.1	n.a	n.a	n.a
COV-02-07	Dripwater	26/06/2012	n.a		-4.1	<0.3	-19.4	<2	13.3	n.a	n.a	n.a
		AVG ± 1SD	**-2.2**	**±0.3**	**-3.8**	**±0.7**	**-17.0**	**±6.5**	**13±2**	**17±3**	**1.8±1.1**	**4.5±3.2**
COV-03	Infiltration-discharge	04/04/2012	n.a	n.a	-5.6	<0.3	-32.2	<2	12.9	n.a	n.a	n.a
FE-01	Infiltration-discharge	21/03/2012	n.a	n.a	-5.7	<0.3	-31.1	<2	14.7	n.a	2.18	n.a
		AVG ± 1SD			**-5.7**	**±0.1**	**-31.7**	**±0.8**	**13.8±1.3**	**n.a**	**2.2**	**n.a**

Table 3

Table 4

Station	Location	T_{mean} (^{o}C ±1SD)	T_{max} (^{o}C)	T_{min} (^{o}C)	T_{winter} (^{o}C)	RH_{mean} (% ±1SD)	RH_{min} (%)	RH_{winter} (%)
Exterior	Exterior	17.7±7.0	37.6	1.5	12.4±4.3	68±19	19	70±18
S1	Upper Bosque Gallery	15.1±2.5	22.5	10.3	12.9±1.4	87±9	21	82±8
S2	Lower Bosque Gallery	13.0±1.1	14.4	9.5	12.1±1.0	95±5	21	92±4
S3	Nieves Gallery	8.7±2.2	13.5	1.0	6.8±2.3	-	-	-

Table 4

Background dataset for online publication only
Click here to download Background dataset for online publication only: SUPPLEMENTARY MATERIAL.docx